ACS APPLIED NANO MATERIALS

www.acsanm.org

Article

Nanoparticles of $Cs_3Bi_2Br_9$ Decorated on $H_2Ti_3O_7$ Nanotubes for the Photocatalytic Oxidation of Hydroxymethylfurfural to 2,5-Furandicarboxaldehyde

Huzaikha Awang, Abdo Hezam, Shuoping Ding, Tim Peppel,* and Jennifer Strunk*

Cite This: *ACS Appl. Nano Mater.* 2024, 7, 25345−25359

Read Online

ACCESS | Metrics & More | Article Recommendations | Supporting Information

ABSTRACT: Herein, the successful construction of heterostructure $Cs_3Bi_2Br_9/H_2Ti_3O_7$ (CBB/HTiO-NT) consisting of nanoparticles of lead-free halide perovskite $Cs_3Bi_2Br_9$ (CBB) on hydrogen titanate nanotubes ($H_2Ti_3O_7$, HTiO-NT) is reported. The application of this heterostructure was intensively investigated in the photocatalytically induced selective oxidation of hydroxymethylfurfural (HMF) to 2,5-furandicarboxaldehyde (FDC) and of benzyl alcohol (BnOH) to benzoic acid (BzA). The weight % (wt %) of CBB nanoparticles was optimized, and the resulting optimal CBB/HTiO-NT heterostructure was deeply analyzed. Comprehensive analysis of the morphology and structure demonstrated the successful combination of HTiO-NT and CBB in CBB/HTiO-NT heterostructures. If the CBB content is too low, it is not stable, potentially because it decomposes at the interface with HTiO-NT. The 30 wt % CBB/HTiO-NT heterojunction exhibited the most efficient photooxidation of HMF and BnOH, with selectivity of 87% for FDC and 81% for BzA, respectively, in an organic solution irradiated by blue light. Analysis of optical and photoelectrochemical properties revealed that the inclusion of CBB nanoparticles into HTiO-NT led to enhanced mobility of charge carriers and improved photocatalytic efficiency. The oxidative characteristics and rate of charge carrier migration in the CBB/HTiO-NT heterostructure were enhanced by the geometry and tubular structure of HTiO-NT, thereby promoting the formation of superoxide ($\cdot O_2^-$) radicals. Furthermore, scavenger experiments have demonstrated the essential role of the photogenerated species, specifically h^+, e^-, and $\cdot O_2^-$, in the process of HMF photooxidation. Consequently, a plausible chemical pathway for the photocatalytic oxidation of HMF to FDC was presented. However, additional improvement of the stability of the composite material is necessary. The present study offers a potential approach to improve photocatalytic conversions to value-added chemicals by utilizing CBB/HTiO-NT-based photocatalysts.

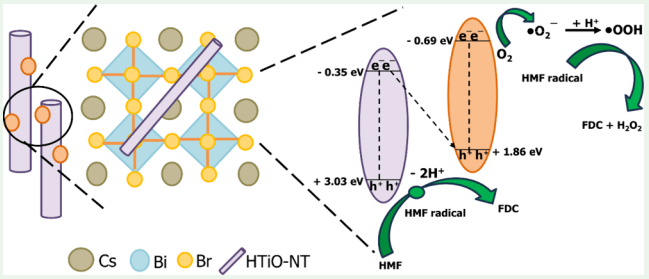

KEYWORDS: *Lead-free Halide Perovskite, Hydrogen Titanate, Photocatalysis, Heterostructure, Hydroxymethylfurfural, 2,5-Furandicarboxaldehyde*

INTRODUCTION

Increasing income, urbanization, and improved electrical accessibility lead to a growing need for global energy,[1] thereby directly causing higher energy-related carbon dioxide emissions through the use of coal, liquid fuels, and natural gas. Therefore, focusing on renewable energy sources and applying photocatalytic technologies is beneficial to meet the global energy demand and avoid future growth of global CO_2 emissions.[2] Heterogenous photocatalysis, with its potentially "green" reaction routes by application of suitable semiconductor materials, has attracted interest in the domains of energy and environmental research such as organic synthesis, environmental remediation,[3] CO_2 reduction,[4] and water splitting.[5] The band structure of semiconductors enables them to absorb photons from irradiation sources and produce electron−hole pairs, hence initiating the photocatalytic process. Numerous investigations have been conducted on several semiconductor materials in recent decades. Nevertheless, the limited ability to capture light and the effectiveness of converting light keep these processes in the experimental stage.[6−10] Cesium bismuth halide perovskites ($Cs_3Bi_2X_9$, X = Cl, Br, I), lead-free materials, are the main focus of this work due to their exceptional optical absorption, changeable band gaps, low toxicity, and good stability compared to other inorganic halide perovskites.[11−13] Nonetheless, the instability of halide perovskites in polar solvents and limited charge carrier mobility have impeded their practical implementation.[14−17] The design of a heterojunction is an effective way to improve the efficiency of charge carrier

Received: July 12, 2024
Revised: September 26, 2024
Accepted: September 27, 2024
Published: October 12, 2024

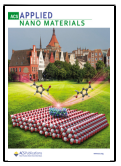

Scheme 1. Pathways for the Synthesis of Various Essential Monomers Derived from HMF[47]

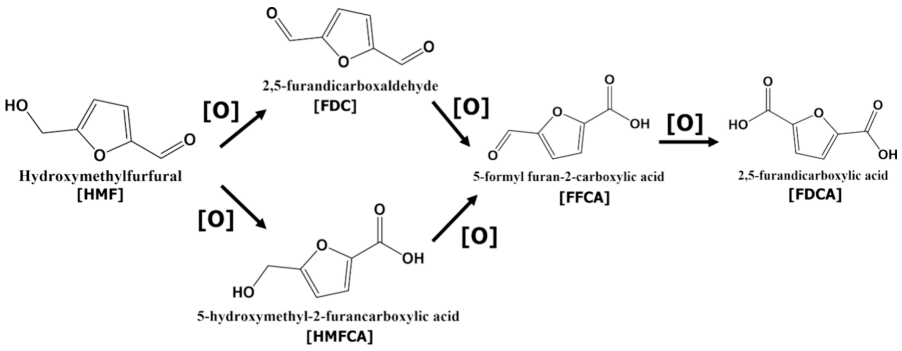

separation and to optimize the light harvesting and absorption capacities. Consequently, this can enhance the redox capacities of the heterostructure.[18,19]

Nanoparticles of hydrogen titanate, denoted as $H_2Ti_xO_{2x+1}$, are receiving significant attention in several fields owing to their unique forms, modifiable band structures, capacity to exchange cations in aqueous solution, excellent physicochemical characteristics, and substantial specific surface areas.[20−22] The size, geometry, and quantum confinement effects primarily affect the free motion of charge carriers (phonons and photons) and the transport properties of the nanomaterials.[23,24] The different sizes and shapes of semiconductors can be classified into various dimensionality.[25,26] To be classified as a nanomaterial, it should be in the nanoscale size (between 1 and 100 nm)[27] in at least one of the three dimensions.[28] For instance, two-dimensional (2D) nanomaterials such as plate-like shapes (nanosheets) have 1 dimension (x) in the nanoscale range and exhibit the quantum confinement effect.[25,26] Nanotubes and nanowires are one-dimensional (1D) nanomaterials, displaying quantum confinement effects because two of their three dimensions are in the nanoscale range.[25,26]

1D hydrogen titanate nanotubes (HTiO-NT) have been extensively studied due to their tubular framework, quantum confinement effects, and large surface area, which guide electron and proton migration and enhance its photocatalytic performance.[29−31] The significant specific pore volume (0.25−1.10 cm^3/g)[32] and surface area (100−500 m^2/g)[33] of HTiO-NT enhance the efficiency of photocatalytic reactions by providing more reaction sites. Moreover, the narrow wall, measuring between 5 and 15 nm in outer diameter and 2 to 6 nm in wall thickness, facilitates fast movement of charges toward the surface of the titanate nanotubes.[23,34,35] Furthermore, HTiO-NTs exhibit distinctive ion-exchange properties due to their layered composition and the increased mobility of protons inside the interlayers.[23]

Previous reports have demonstrated the fabrication of heterojunctions utilizing halide perovskites in conjunction with titanates and graphitic carbon nitride (g-C_3N_4). Enhanced oxidation of benzyl alcohol has been achieved using $CsPbBr_3/TiO_2$ and $Cs_3Bi_2Br_9/TiO_2$, as compared to the pristine perovskites.[36−38] The combination of $Cs_3Bi_2Br_9$/g-C_3N_4 composites has significantly improved the effectiveness of photocatalytic degradation of rhodamine B (RhB).[39] Our earlier study demonstrated that the combination of $Cs_3Bi_2Br_9$ (CBB) perovskite and hydrogen titanate nanosheets (HTiO-NS) in a heterostructure resulted in improved BnOH photooxidation efficiency.[40] Compared to the original CBB and HTiO-NS, the HTiO-NS exhibited a 98% conversion rate and a 75% selectivity toward BzA. This study has successfully shown that the incorporation of CBB and HTiO-NS nanoparticles has broadened the spectrum of visible-light responsiveness and enhanced the mobility of free electrons. The oxidative characteristics have been enhanced by the incorporation of HTiO-NS, potentially through charge separation at the heterojunction.[40]

Transformation reactions of hydroxymethylfurfural (HMF) to produce value-added chemicals have recently become a hot topic among the scientific community. HMF is conveniently obtained as dehydration product of C_6 carbohydrates sourced from biomass, potentially from abundant and inexpensive glucose molecules generated from lignocellulose.[41] The structure of HMF with its furanic ring and the attached −OH and −CHO functional groups (refer to Scheme 1) facilitates the formation of several important chemicals such as maleic anhydride (MA), 2,5-furandicarboxaldehyde (FDC), 5-formyl-2-furancarboxylic acid (FFCA), 5-hydroxymethyl-2-furancarboxylic acid (HFCA), and 2,5-furandicarboxylic acid (FDCA). These compounds have a vital role as essential raw materials in the pharmaceutical and polymer industries.[42,43] FDC is an essential monomer for furyl polymers, pharmaceutical intermediates, and antimicrobials.[44] Recent reports indicate that the distribution of products during the partial oxidation of HMF can be complicated and highly difficult due to the susceptibility of the −CHO and −OH functional groups in the derivatives to further oxidize under identical reaction conditions. Generally, thermocatalytic approaches need energy-intensive and expensive noble metal catalysts, making these methods environmentally unfriendly.[45] Instead, the application of heterogeneous photocatalysis technology via selective redox processes can be beneficial due to the lower energy consumption, environmental friendliness, and cost efficiency.[46]

Here, we propose a direct method to address the restricted mobility of charge carriers in the CBB by creating a CBB/HTiO-NT heterostructure. The ideal CBB/HTiO-NT heterostructures were effectively created by adjusting the quantities of CBB nanoparticles and incorporating the HTiO-NT via a modified antisolvent reprecipitation approach. The objective of this work is to expand the spectrum of visible-light responsiveness, improve the mobility of charge carriers, and optimize the oxidative properties of the heterostructures. The primary goal of this work is to enhance the photocatalytic performance of the CBB/HTiO-NT heterostructure. The CBB/HTiO-NT structure performed effectively in the selective photocatalytic oxidation of HMF to FDC and

https://doi.org/10.1021/acsanm.4c03998
ACS Appl. Nano Mater. 2024, 7, 25345−25359

Scheme 2. Schematic Depiction for the Synthesis of (a) HTiO-NT and (b) CBB/HTiO-NT Heterostructures

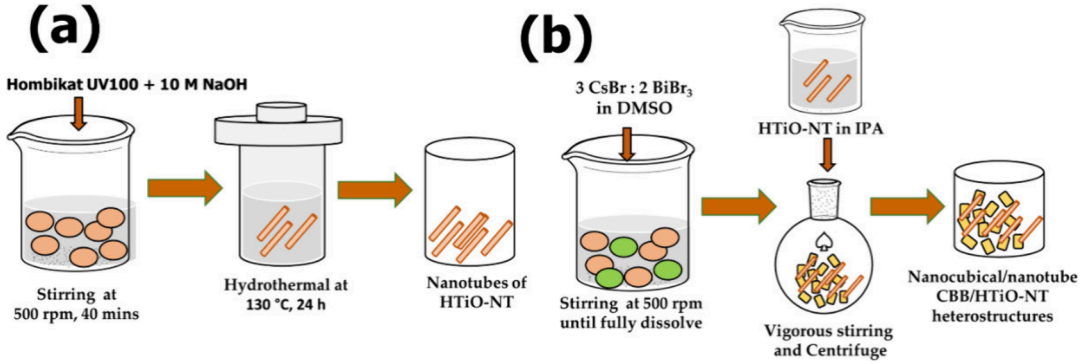

BnOH to BzA. Our observations indicate that the 30 wt % $Cs_3Bi_2Br_9$/HTiO-NT exhibited the most efficient photooxidation performance for HMF and BnOH, with selectivity of 87% for FDC and 81% for BzA. The optimal heterostructure improved the HMF photooxidation performance with 87% FDC selectivity compared to 47% and 14% for pristine CBB and HTiO-NT, respectively. In conclusion, by successfully synthesizing and thoroughly characterizing the HTiO-NT and CBB/HTiO-NT heterostructures, we have established their functions in the composite. The enhanced photocatalytic efficiency seen in this work can be attributed generally to the (1) tubular framework of HTiO-NT, (2) excellent optical properties of CBB nanoparticles, and (3) the band matching and synergistic interaction between CBB and HTiO-NT, which lead to enhancing the charge density to facilitate rapid charge carrier migration. This work proposes a method for utilizing HTNM-based photocatalysts to enhance the flow of charge carriers and the photocatalytic efficiency of CBB. Furthermore, scavenger tests revealed that the h^+, e^- and $\cdot O_2^-$, are crucial in the photooxidation of HMF. In this work, novel concepts for hydrogen titanate-based heterostructures and photocatalytic conversion of biomass to compounds with added value are presented.

EXPERIMENTAL SECTION

Materials. HTiO-NT, CBB, and CBB/HTiO-NT heterostructures were prepared using Hombikat UV100 (Venator, Wynyard, UK), sodium hydroxide (NaOH, Fischer Scientific, Hampton, NH, USA), hydrochloric acid (HCl, 37%, Fischer Scientific), deionized water (DI), bismuth bromide ($BiBr_3$, Sigma-Aldrich, St. Louis, MO, USA), cesium bromide (CsBr, Sigma-Aldrich), dimethyl sulfoxide (DMSO, Sigma-Aldrich), and isopropanol (IPA, Sigma-Aldrich). HMF and BnOH oxidation studies were conducted using hydroxymethylfurfural (HMF) and 2,5-furandicarboxaldehyde (FDC), benzyl alcohol (BnOH, Sigma-Aldrich), acetonitrile (MeCN, Sigma-Aldrich), and 1,2-dichlorobenzene (DCB, Sigma-Aldrich). The scavenger experiment was conducted using potassium iodide (KI, Sigma-Aldrich), silver nitrate ($AgNO_3$, Sigma-Aldrich), *p*-benzoquinone (*p*-BQ, Sigma-Aldrich), and tert-butyl alcohol (TBA Sigma-Aldrich). The chemical reagents with purities over 99% were used without further purification.

Synthesis of HTiO-NT. Scheme 2a demonstrates the synthesis of hydrogen titanate nanotubes (HTiO-NT) as described in our earlier publication, with some modifications.[40] HTiO-NT were synthesized via a hydrothermal process using a concentrated 10 M NaOH solution and UV100. A mass of 1.00 g of UV100 was suspended into 70 mL of 10 M NaOH solution and exposed to ultrasonication at ambient temperature for an hour. The mixture was stirred at ambient temperature for 1 h at a speed of 500 rpm and then placed in a stainless-steel autoclave lined with PTFE, securely sealed, and maintained at 130 °C for 24 h. Afterward, the hydrogen titanate was rinsed with DI water and a 0.1 M HCl aqueous solution and then filtered by centrifugation. Washing was repeated until the filtrate showed a pH value below 7. The colorless solids were dried in an oven at 70 °C and then stored as HTiO-NT. The solid HTiO-NT amounted to a mass of 0.74 g.

Synthesis of $Cs_3Bi_2Br_9$ (CBB). Scheme 2b shows the preparation of CBB via a modified antisolvent reprecipitation method without adding the HTiO-NT. In 20 mL of DMSO, 192.0 mg of CsBr and 269.0 mg of $BiBr_3$ were dissolved and stirred at 500 rpm at room temperature. The mixture was put into 500 mL of IPA and stirred vigorously at room temperature for 10 min. The resultant precursor mixture was centrifuged at 3,000 rpm for 3 min, followed by centrifugation at 10,000 rpm for 5 min using IPA. The obtained yellow solids were then vacuum-dried at 60 °C overnight (p < 70 mbar) and stored as CBB (yield: 335.0 mg, 73%). Elemental analysis for synthesized CBB in % (calc.): Cs 21.5 (26.0), Bi 27.1 (27.2), Br 35.6 (46.8).

Synthesis of CBB/HTiO-NT Heterostructures. Scheme 2b illustrates the preparation of the CBB/HTiO-NT heterostructures. CBB of various weight percentages (wt %) was used to form a set of different heterostructures (10, 30, and 50 wt %). First, 123.6 mg of CsBr and 173.8 mg of $BiBr_3$ were dissolved in 12.9 mL of DMSO to form a 30 wt % CBB precursor solution (mixture A). At room temperature, mixture A was stirred at 500 rpm until no remaining solids were observed. Next, 500.0 mg of HTiO-NT was added to 500 mL of IPA (mixture B). Ultrasonication and stirring of mixture B was carried out for 30 and 5 min, respectively, at room temperature. Subsequently, mixture A was rapidly injected into mixture B while being subjected to vigorous stirring, and the combination was stirred continuously for 10 min. The resultant mixture was centrifuged at 3,000 rpm for 3 min and at 10,000 rpm for 5 min using IPA. The obtained yellow solids were then vacuum-dried at 60 °C (p < 70 mbar) overnight and stored as CBB/HTiO-NT-30. The same procedure was repeated to synthesize CBB/HTiO-NT-10 (10 wt %) and CBB/HTiO-NT-50 (50 wt %) heterostructures. Elemental analysis for synthesized CBB/HTiO-NT-10 in % (calc.): Ti 43.4 (46.5), Cs 3.3 (4.3), Bi 4.5 (4.5), Br 3.8 (7.8); CBB/HTiO-NT-30: Ti 32.5 (34.9), Cs 7.6 (9.7), Bi 10.1 (10.2), Br 12.6 (17.5); CBB/HTiO-NT-50: Ti 26.7 (28.0), Cs 9.9 (13.0), Bi 13.7 (13.6), Br 17.5 (22.3).

Characterizations. The elemental analysis of Bi, Ti, and Na was performed using an ICP-OES device (Anton Paar, Graz, Austria/PerkinElmer, Waltham, MA, USA). The Br content was determined by potentiometric titration (Titrator Excellence T7, Mettler Toledo, Columbus, OH, USA). Cs content was determined by atomic absorption spectroscopy (AAS, PerkinElmer AAS-AAnalyst 300 spectrometers). SEM micrographs were generated by using a Merlin VP compact device (Zeiss, Oberkochen, Germany). The EDX was measured by using a Bruker Quantax device (Billerica, MA, USA). TEM and HRTEM images were recorded using a JEOL, JEM-ARM200F device (Freising, Germany) operated at an acceleration voltage of 200 kV. The crystalline phases were measured via Powder

https://doi.org/10.1021/acsanm.4c03998
ACS Appl. Nano Mater. 2024, 7, 25345−25359

X-ray diffraction (p-XRD, Xpert Pro diffractometer, PANanalytical, Almelo, The Netherlands; Xcelerator detector with automatic divergence slits and $CuK_{\alpha 1}K_{\alpha 2}$ radiation, 40 kV, 40 mA; λ_1 = 0.15406 nm; λ_2 = 0.15443 nm). The obtained intensities were converted from automatic to fixed divergence slits (0.25°) for further analysis. The phase identification was done using the International Center of Diffraction Data (ICDD) database. X-ray photoelectron spectroscopy (XPS) was used to measure the surface and chemical components. A photoelectron spectrometer (Multilab 2000, Thermo Fisher, Waltham, MA, USA) with Al K_α radiation as the excitation source was used. All XP spectra were referenced to the C 1s line at 284.6 eV. Specific surface areas of the synthesized photocatalysts were identified by using the Brunauer–Emmett–Teller (BET) method with BELSORP max II (Microtrac Retsch GmbH, Haan, Germany) and NOVAtouch (Anton Paar Germany GmbH, Ostfildern-Scharnhausen, Germany) devices. Prior to measurement, all prepared samples were degassed at 200 °C for a duration of 5 h.

Photocatalytic Oxidations. The photocatalytic oxidation processes of HMF and BnOH were conducted in 5 mL glass vials powered by a 5 W blue light-emitting diode at ambient temperature and subjected to magnetic stirring at 500 rpm. The light intensity of the blue LEDs was 25 mW cm^{-2}, and the maximum wavelength was 467 nm. A 5 mM solution of HMF was prepared with acetonitrile (CH_3CN) as the base solvent. For each experiment, 10 mg of photocatalyst was evenly distributed in 2 mL of HMF solution and then subjected to a 10 min oxygen purging process at a flow rate of 10.8 mL min^{-1}. The solution was agitated at 500 rpm in the absence of light, while the airflow of the fan was adjusted to sustain ambient temperature for a duration of 30 min. Afterward, the solution was irradiated with the 5 W blue LEDs at room temperature for 1.5 h. Following each reaction, the samples were passed through a 0.22 mm filter for further analysis. The specimen were diluted by a factor of 20 with water to a volume of 1 mL and then subjected to analysis using high-performance liquid chromatography (HPLC, Agilent Technologies, 1260 Infinity Series, Santa Clara, CA, USA). The HPLC instrument was fitted with a 300 mm section of organic acid resin column with an inner diameter of 7.80 mm (Rezex ROA-Organic Acid, 00H-0138-K). The mobile phase consisted of a 2 mM trifluoroacetic acid (TFA) solution dissolved in 1 L of aqueous solution (149 μL of TFA) at a flow rate of 0.6 mL min^{-1} at a temperature of 40 °C. The injection volume was 10 μL. The furan compounds were detected by a diode array detector (DAD) at 270 nm according to the different retention times and response peak areas. The retention durations of HMF, FDC, and FFCA were approximately 36.7, 45.8, and 16.75 min, respectively. The quantification of furan compounds was conducted based on the external standard calibration curves reported in our previous work.[47] The photocatalytic oxidation of BnOH was carried out with a 20 mM solution of BnOH, which was prepared using acetonitrile (CH_3CN) as the solvent. Ten mg of photocatalyst was evenly mixed in 2 mL of BnOH solution in each experiment. The solution was subsequently purged with oxygen for 10 min at a flow rate of 10.8 mL min^{-1} and then agitated at 500 rpm for 30 min in the absence of light. Subsequently, the samples were exposed to 5 W blue LEDs while being stirred at 500 rpm for 2 h. The reactants and products were analyzed using gas chromatography (GC, Agilent 19091X-133) in conjunction with a flame ionization detector (FID). This study used a capillary column 30 m in length, with an inner diameter of 0.25 mm and a film thickness of 0.25 μm. The column temperature was initially fixed at 60 °C for 5 min and then successively raised to 240 °C at a rate of 15 K min^{-1}, with a final holding duration of 5 min. The chromatograms were acquired by the injection of 1 μL of the material. This study presents the quantitative data of oxidation products obtained using the internal standard approach. (1) Following each reaction, the samples were collected and filtered using a 0.22 mm filter. (2) The 0.5 μL samples were diluted with 0.5 μL of DCB (internal standard) in a GC vial. (3) The diluted solution was then injected into the GC instrument to quantify the oxidation products based on their retention times and response peak areas. The retention durations of BnOH, BzH, and BzA were approximately 15.60, 12.63, and 19.31 min, respectively. Finally, the calculation of the conversion, selectivity, yield, and conversion rate of HMF and BnOH oxidation was performed as given by eqs S1–S4. To assess the photocatalytic stability, the photocatalyst was obtained by centrifugation at 8000 rpm after the reaction was completed. Next, the obtained photocatalyst was thoroughly rinsed with ethanol multiple times. The collected residue was dried in a vacuum oven set at a temperature of 60 °C and afterward reused for the second cycle. To conduct the reaction in the second run, 10 mg of the photocatalyst used prior was evenly mixed in 2 mL of HMF solution.

Mechanism Characterization and Experiments. Using UV–vis spectroscopy in diffuse reflectance (DRS, Lambda 365, PerkinElmer, Waltham, MA, USA), the absorption edges of the photocatalyst were determined throughout a wavelength range of 190 to 1100 nm. The bandgap energy of the photocatalyst was determined using a standard Tauc plot and applying the Kubelka–Munk equation (eq S5). A Zennium electrochemical workstation, equipped with a PP211 CIMPS system (Zahner, Kronach, Germany), was used to conduct photoelectrochemical experiments. The workstation employed a standard three-electrode cell and a 430 nm LED lamp (400 mW/cm^2) as the light source. The reference electrodes consisted of Ag/AgCl solution (3 M, NaCl) that was saturated, whereas the counter electrodes utilized platinum wire. The electrolyte was a 0.1 M solution of tetra-*n*-butyl hexafluorosphate in dichloromethane. The electrode was fabricated via the application of a coating technique. Initially, a 100 μL Nafion solution (5 wt %) and 900 μL IPA were mixed with 20 mg of photocatalyst and subjected to ultrasonic treatment for 10 min. Subsequently, the dispersion was spread onto a 1.5 × 1.5 cm^2 FTO glass surface and allowed to dry overnight in ambient air. Electrochemical impedance spectroscopy (EIS) was conducted using a potential static technique operating within the frequency range of 0.01 to 100 kHz. Using electrochemical impedance measurements, the Mott–Schottky curves were obtained to examine the flat-band potential of the photocatalyst. The conduction band (CB) and valence band (VB) of n-type semiconductors, HTiO-NT, were determined by eq S6. The E_{CB} is the CB energy, $E^0_{(Ag/AgCl)}$ is the standard electrode potential which is +0.209 V for Ag/AgCl at 25 °C at pH 7.

Scavenger Experiment (Reactive Oxygen Species Monitoring). The scavenger test was employed to examine the reactive oxygen species (ROSs) significantly involved in the conversion of HMF. The conditions and procedures outlined in the section on photocatalytic oxidations were implemented in the scavenger experiments. The photogenerated holes (h^+),[48] electrons (e^-),[49] superoxide radical ($\cdot O_2^-$),[37,50] and hydroxyl radical ($\cdot OH$)[48] were suppressed by using KI, $AgNO_3$, *p*-BQ, and TBA scavengers, respectively. In each HMF oxidation reaction, a 3 mM scavenger substance was added, and the influence of that scavenger on the reaction was further analyzed. In general, a decline in photocatalytic performance in the presence of scavengers demonstrates the importance of the reactive species.

RESULTS AND DISCUSSION

Synthesis of Heterostructures. CBB, HTiO-NT, and CBB/HTiO-NT heterostructures, respectively, were synthesized via a facile synthetic route in high yields (see Experimental Section). Values from elemental analyses of HTiO-NT and CBB/HTiO-NT heterostructures can be found in Experimental Section and in Table S1. The contents of Cs, Bi, and Br obtained for pristine CBB resemble closely those reported previously.[40] The results for pristine HTiO-NT showed an amount of H ∼1 wt %. The addition of a greater weight % of CBB to the HTiO-NT results in increased concentrations of Cs, Bi, and Br, while reducing the Ti content. Minor sodium impurities (<1.4 wt %) were seen in CBB/HTiO-NT heterostructures as a result of the excessive use of NaOH solvent during hydrothermal procedures. The remain-

https://doi.org/10.1021/acsanm.4c03998
ACS Appl. Nano Mater. 2024, 7, 25345–25359

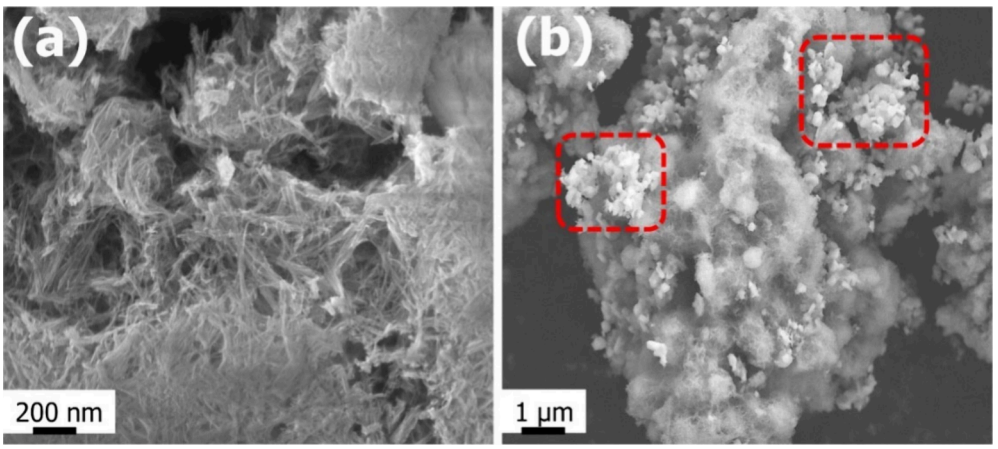

Figure 1. SEM micrographs of (a) HTiO-NT at high magnifications and (b) overview of CBB/HTiO-NT-30 heterostructure with red boxes highlighting areas with prevalence of CBB particles.

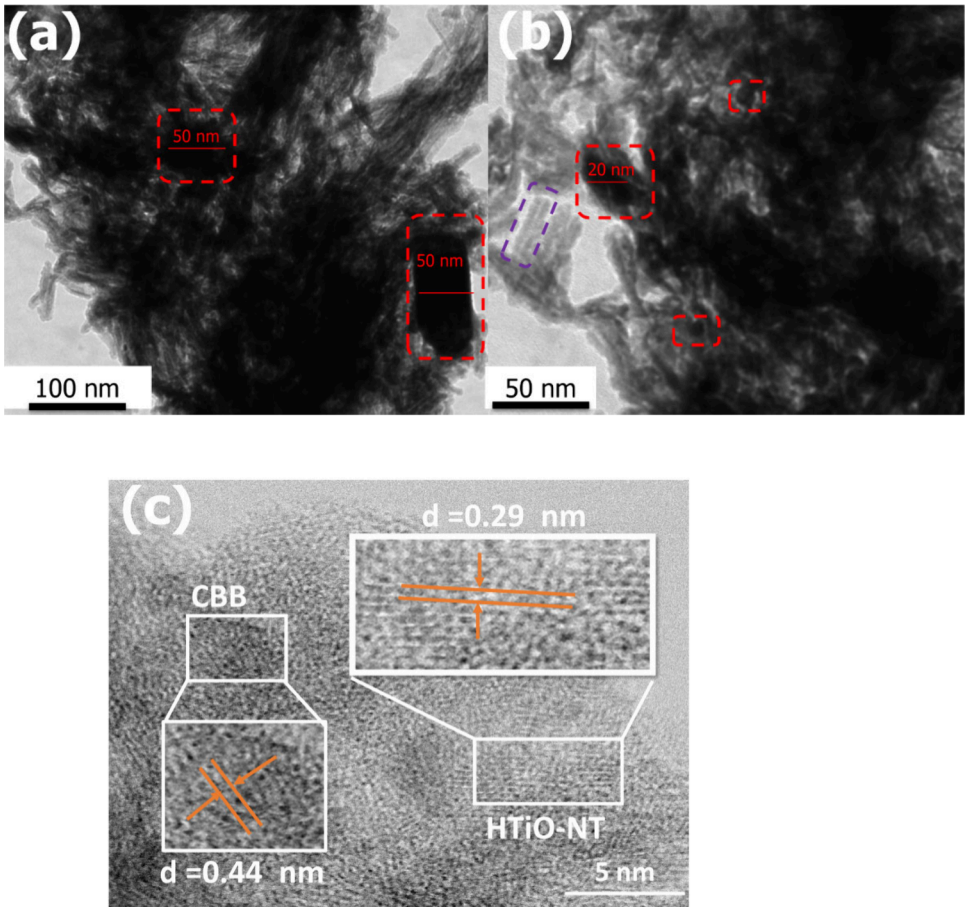

Figure 2. (a and b) TEM images of CBB/HTiO-NT-30 heterostructure with HTiO-NT in purple box and possible CBB in red boxes and (c) HRTEM image of the CBB/HTiO-NT-30 heterostructure.

ing weight percent consists solely of oxygen, as indicated by the XPS and EDX data.

Morphology and Structure Characterization. SEM micrographs of HTiO-NT and CBB/HTiO-NT-30 are depicted in Figure 1. Figure 1a shows the needle-shaped HTiO-NT similar to the previous study, which uses a similar synthesis method.[23,51,52] The highly developed fiber-like and tubular framework growth of HTiO-NT suggests higher structural stability and charge carrier mobility, which might enhance and stabilize the photocatalytic system.[29−31,53] From Figure 1b it is obvious that the nanotube morphology of HTiO-NT remained intact by modification with 30 wt % CBB. It can be concluded that the distribution of CBB onto the HTiO-NT is rather inhomogeneous leading to areas with almost no CBB concentration and areas of very high CBB concentrations (see red markers in Figure 1b).

Additional SEM images, EDX images, and elemental mapping of CBB and CBB/HTiO-NT heterostructures, respectively, can be found in Figure S1. Figure S1a,b shows

https://doi.org/10.1021/acsanm.4c03998
ACS Appl. Nano Mater. 2024, 7, 25345−25359

the cubical structure and EDX of pure CBB (average crystallite sizes ~200−300 nm), as reported in our previous work.[40]

TEM investigations of CBB/HTiO-NT-30 (Figure 2) further showed the highly dispersed tubular shape of HTiO-NT (see the purple box in Figure 2b) and the dark cubical structure of CBB (see the red boxes in Figure 2a,b). The CBB nanoparticles in the CBB/HTiO-NT heterostructure showed a smaller diameter of about 20−50 nm compared to 200−300 nm for pure CBB (see Figure S1a). The HRTEM images (Figure 2c) revealed the CBB-decorated HTiO-NT with lattice fringes measuring approximately 0.44 and 0.29 nm, respectively. Therefore, the SEM-EDX, TEM, and HRTEM findings verified the presence of CBB and HTiO-NT and demonstrated the formation of CBB/HTiO-NT heterostructures. Results from the pXRD are depicted in Figure 3. The diffraction

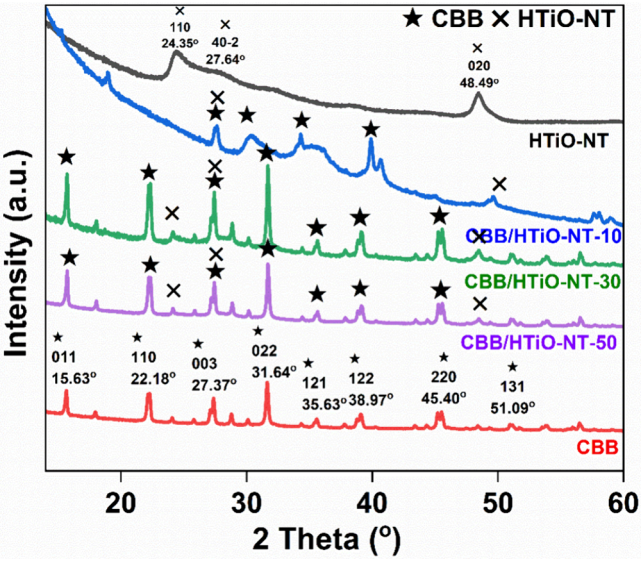

Figure 3. pXRD patterns of HTiO-NT, CBB, and CBB/HTiO-NT heterostructures.

patterns of HTiO-NT and CBB exhibited distinctive reflexes which were mostly in accordance to reference materials ($H_2Ti_3O_7$, JCPDS 021-1272; CBB, JCPDS 01-070-0493).[4,52,54−57] The weak peak is related to the low crystallinity of the formed nanotube hydrogen titanate. The weak pXRD peak at 24.35 for HTiO-NT is related to the low crystallinity of formed nanotube hydrogen titanate, similar to that reported by previous studies.[58,59] Ref 59 reveals that a significant amount of Na^+ cations and highly basic conditions are crucial for the formation of HTiO nanotubes. Very sharp diffraction peaks can be obtained when replacing NaOH with KOH, but the SEM shows that the morphology is plates and nanorods. The powder patterns of samples CBB/HTiO-NT-30 and CBB/HTiO-NT-50 displayed similar features without forming other interphases. The intensity of the peaks of CBB was very high at these loadings, similar to those reported in a previous study.[37] pXRD patterns of the composites rarely exhibit the hydrogen titanate pattern due to the large molecular weight and substantial X-ray absorption and scattering of bismuth. The XRD pattern of CBB/HTiO-NT-10 deviates from those of the other samples. The CBB reflexes are poorly observable, and they are also shifted. As explained in more detail below, the CBB is not stable in the presence of water. It is suspected that the very hydrophilic and OH-group-terminated titanate nanotubes might foster the degradation of CBB directly attached to them. If the loading of CBB is low, such processes will be more significant than at higher CBB loadings—and conversely at lower contents of HTiO-NT.

Characterization of the elemental compositions and surface chemical states of HTiO-NT, CBB, and CBB/HTiO-NT-30 was conducted by XPS measurements, as shown in Figure 4. The Ti 2p spectra of HTiO-NT (Figure 4b) exhibited two resonance peaks at 464.7 and 472.1 eV, corresponding to Ti $2p_{1/2}$ and Ti $2p_{3/2}$ species, respectively.[9] The CBB/HTiO-NT heterostructure showed similar peaks as of the HTiO-NT at 464.5 and 471.8 eV. In comparison to the pristine CBB, the binding energies of Cs 3d (Figure 4c) and Bi 4f (Figure 4d) exhibited a negative shift. At a binding energy of 724.6 eV, the Cs 3d spectra for CBB corresponds to Cs $3d_{5/2}$ species, while at 738.4 eV it corresponds to Cs $3d_{3/2}$ species.[60] The Cs 3d XPS peaks of the CBB/HTiO-NT heterostructure exhibited a shift to energy levels of 720.2 and 734.2 eV, respectively. Bi 4f spectra of CBB displayed two peaks with binding energies at 159.3 and 164.6 eV, corresponding to Bi $4f_{7/2}$ and Bi $4f_{5/2}$, respectively.[61]

The Bi 4f XPS spectrum of CBB/HTiO-NT was shifted to 158.1 and 163.5 eV, respectively. In Figure 4e, the Br 3d spectra of CBB exhibited binding energies of 68.6 and 69.6 eV. The CBB/HTiO-NT peaks were observed at 69.4 eV. The significant negative shift of CBB/HTiO-NT peaks for Cs 3d (Figure 4c) and Bi 4f (Figure 4d) as compared to the CBB, respectively, confirmed the charge transfer between HTiO-NT and CBB via these bonds.[62,63]

Figure S2 depicts the nitrogen adsorption−desorption isotherms of the photocatalyst, and the inset table depicts the surface area, pore size, and pore volume, which were analyzed via BET measurement. In the pressure range of 0.7−1.9 P/P_0, the adsorption−desorption isotherm results of HTiO-NT and CBB/HTiO-NT heterostructures showed characteristic type IV isotherms with substantial adsorption capacities, suggesting the existence of numerous mesopores (2−50 nm) in the photocatalyst.[64−66] An analysis of HTiO-NT revealed a surface area of 250 m^2/g, a pore size of 1.7 nm, and a pore volume of 0.3 cm^3/g. Specifically, the surface areas of CBB/HTiO-NT-10, CBB/HTiO-NT-30, and CBB/HTiO-NT-50 were measured to be 259 m^2/g, 169 m^2/g, and 137 m^2/g, respectively. The decrease in surface areas with higher loadings of CBB is a direct indication of the excessive aggregation of the latter onto the surface of HTiO-NT. This behavior is in accordance with findings from the SEM investigation (see above).[67] The enhanced photocatalytic activity of HTiO-NT and CBB/HTiO-NT heterostructures can be attributed to their increased specific surface areas and reduced pore volumes.[32,33]

Photocatalytic Performance. The HMF photooxidation performance for CBB, HTiO-NT, CBB/HTiO-NT heterostructures, and the reference without catalyst ("No Catalyst") is shown in Figure 5a at 1.5 h irradiation times. The following important observations could be made from the presented results: At comparable conversions, FDC selectivity was lower for pristine CBB and HTiO-NT compared to CBB/HTiO-NT heterostructures. Almost no conversion was observed when there was no catalyst present. The result proves that the CBB and HTiO-NT already perform well on photocatalytic oxidation even when they are not present as a composite. Second, the CBB/HTiO-NT heterostructures show synergistic effects by enhancing the FDC selectivity compared to pure

https://doi.org/10.1021/acsanm.4c03998
ACS Appl. Nano Mater. 2024, 7, 25345−25359

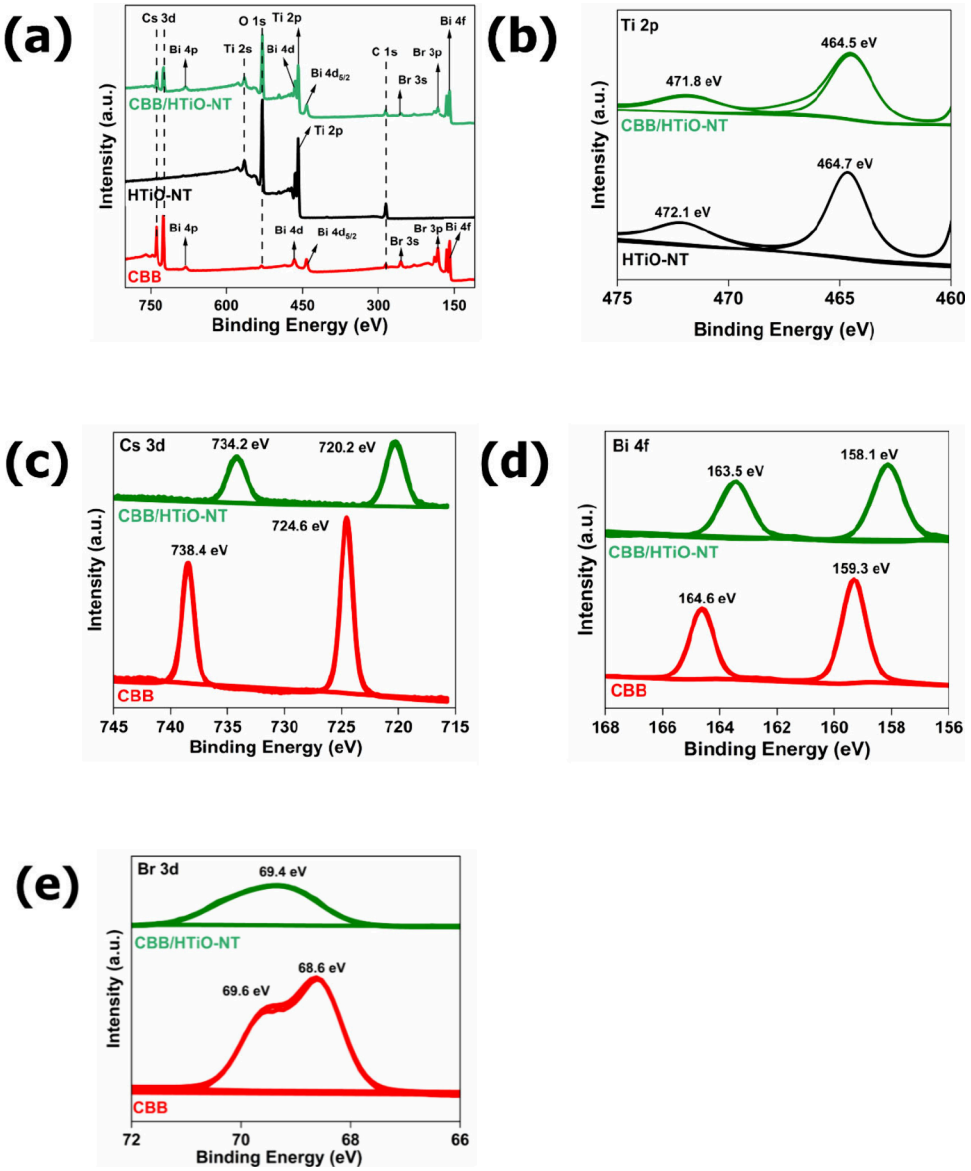

Figure 4. (a) XPS survey spectra for HTiO-NT, CBB, and CBB/HTiO-NT; (b) Ti 2p bands for HTiO-NT and CBB/HTiO-NT; (c) Cs 3d bands; (d) Bi 4f bands; (e) Br 3d bands for CBB and CBB/HTiO-NT heterostructures.

CBB and pure HTiO-NT. The higher the CBB loading in the heterostructure, the higher the FDC selectivity. The improved photocatalytic oxidation by CBB/HTiO-NT heterostructures may be attributed to an enhancement in the oxidative characteristics, perhaps facilitated by charge separation at the heterojunction. Finally, the CBB/HTiO-NT-30 with 87% FDC selectivity appears to be the optimal heterostructure compared to CBB/HTiO-NT-10 and CBB/HTiO-NT-50, which achieved 80% and 71% FDC selectivity, respectively. Reduced FDC selectivity of CBB/HTiO-NT-50 is due to the further oxidation of FDC to 5-formyl furan-2-carboxylic acid (FFCA).[47,68] A summary of the product yield and carbon balance yield (CBY) is provided in Table S3. The CBY is determined by dividing the total yields of the products by the percentage of HMF conversion. The CBB/HTiO-NT-30 heterostructure in its optimum state showed the greatest product yield and CBY, reaching 84% and 87%, respectively. Furthermore, the impact of substrate concentration on the photocatalytic oxidation of HMF toward FDC was investigated, and the findings are presented in Figure 5b. At 2.5 mM HMF concentration, the selectivity of FDC was low, about 15%, and significantly increased to 87% when using 5 mM HMF concentration. The 10 mM and 25 mM HMF concentrations showed decreased FDC selectivity to 66% and 41%, respectively. These results show that the optimal HMF reaction condition for CBB/HTiO-NT-30 was at 1.5 h with 97% HMF conversion and 87% FDC selectivity using 5 mM concentration of HMF. The HMF photooxidation performance proved that the CBB/HTiO-NT heterostructures could perform crucial reactions to produce fine chemicals without using harmful chemical oxidants and costly catalysts. Figure 5c shows the BnOH photooxidation performance of CBB, HTiO-NT, and CBB/HTiO-NT heterostructures and the "No Catalyst" reference measurement. The CBB and HTiO-NT could perform BnOH photooxidation toward BzH with 84% and 44% selectivities, respectively. No BzH was observed without the presence of catalyst. This observation reveals the oxidation ability of CBB and HTiO-NT. In contrast

https://doi.org/10.1021/acsanm.4c03998
ACS Appl. Nano Mater. 2024, 7, 25345−25359

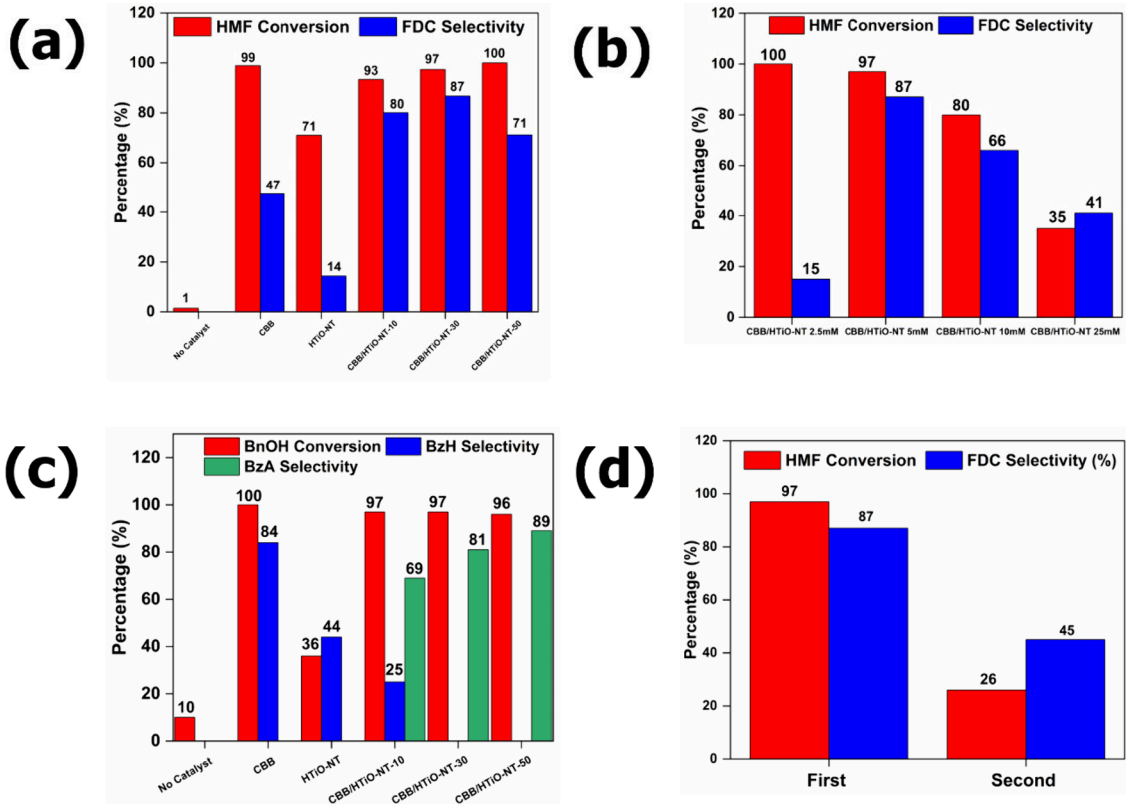

Figure 5. Conversion (red bar) and selectivities (blue bar) of HMF photooxidation toward FDC for (a) No Catalyst, CBB, HTiO-NT and CBB/HTiO-NT heterostructures at 1.5 h, 10 mg of catalyst, and 5 mM concentration of HMF; (b) CBB/HTiO-NT-30 with various HMF concentrations at 1.5 h and 10 mg of catalyst; (c) conversion (red bar), BzH selectivity (blue bar), and BzA selectivity (green bar) of BnOH photooxidation for No Catalyst, CBB, HTiO-NT, and CBB/HTiO-NT heterostructures at 2.0 h, 10 mg of catalyst, and 20 mM concentration of BnOH and (d) conversion (red bar) and selectivities (blue bar) of HMF photooxidation toward FDC for stability measurement of CBB/HTiO-NT heterostructures.

to our previous study, the pristine HTiO-NS was not able to produce BzH at the same reaction conditions.[40] Hence, the alteration of hydrogen titanate shape in this work clearly benefits enhancing the photooxidation activity and achieving an effective heterostructure. The CBB/HTiO-NT-30 was considered to be the optimal heterostructure compared to CBB/HTiO-NT-10 and CBB/HTiO-NT-50. The CBB/HTiO-NT-10 showed a mixture of BzH and BzA oxidation products, which might be due to the low content of CBB (10 wt %), lowering its light absorption ability. Besides that, it is not worth adding 50 wt % of CBB to HTiO-NT for only 8% increased BzA selectivity. The enhanced photocatalytic oxidation of CBB/HTiO-NT heterostructures compared to CBB and HTiO-NT possibly originated from the (1) tubular framework of HTiO-NT, (2) excellent optical properties of CBB, and (3) the band matching and synergistic interaction between CBB and HTiO-NT, which resulted in an optimization of charge density to promote efficient migration of charge carriers. In summary, the improved photooxidation efficiency of HMF and BnOH in CBB/HTiO-NT heterostructures provides further proof of the successful creation of the heterojunctions.

The HMF photooxidation of CBB/HTiO-NT heterostructures in two consecutive cycles is depicted in Figure 5d. The recycling test indicated moderate recyclability, as seen by the decrease in HMF conversion and FDC selectivity during the second cycle. The poor recyclability of perovskite-based photocatalysts was aligned with previous studies for CBHTNS[40] and $CsPbBr_3/TiO_2$.[38] Figures S4, S5, and S6 depict UV−vis DRS, pXRD, and SEM results, respectively, which were used to characterize the postreaction catalyst. Figure S4 illustrates a notable shift in the absorption edge where the postreaction catalyst transitioned from 480 to 410 nm. The observed change could be attributed to alterations in the interface structures of CBB[69] and, more possibly, to the degradation of CBB in the catalyst after the reaction.[70] The reduced amount of CBB can be noticed from the color change, from bright yellow (before reaction) to light yellow (after reaction) in the inset of Figure S4. Through pXRD analysis, it was shown that the peak intensity of the diffraction pattern of CBB diminished to the point that only the peaks of the titanate nanotubes remained visible. SEM confirmed the reduced structure of CBB after the HMF reaction, as shown by the red rectangle in Figure S6, in accordance with the pXRD analysis. The two findings suggest a modification in the composition of the CBB, most likely occurring at the interface, which was considered the primary cause of the low recyclability in the second cycle. Hence, future attempts will be directed toward enhancing the stability of CBB in this system. Integrating CBB with other highly effective semiconductors has the potential to improve its catalytic efficiency and stability.[71] The primary issues that must be addressed in perovskites are their inadequate resistances to both moisture and heat.[69,70,72] Perovskite materials having the ABX_3 formula significantly undergo reactions with water or moisture, resulting in their breakdown into their original components or the formation of

https://doi.org/10.1021/acsanm.4c03998
ACS Appl. Nano Mater. 2024, 7, 25345−25359

hydrated phases.[70] Perovskites are not resistant to dissolving in water and other polar solvents, so they undergo degradation when exposed to moisture or water.[73,74] In contrast, ref 75 indicated that an appropriate amount of moisture is advantageous for the crystallization, grain growth, and distribution of the perovskite layer. However, excessive water harms the crystal structure of the perovskite and leads to its degradation into its initial compounds and hydrated phases.

A comparison of the photocatalytic performance of CBB/HTiO-NT-30 heterostructures as an optimal photocatalyst for BnOH and HMF oxidation with other recent photocatalysts from the literature was also performed. The results are shown in Table S2. It is crucial to acknowledge that the reaction conditions are only slightly similar, which consequently impacts the conversion, selectivities, and generation of the reaction products. The CBB/HTiO-NT-30 catalyst achieved an ideal reaction rate with 97% HMF conversion and 87% FDC selectivity after 1.5 h, using a 5 mM HMF concentration. In the subsequent comparison with prior studies, it is crucial to mention that FDC was commonly denoted as "diformylfuran", abbreviation DFF. At the slightly different reaction conditions, the $ZnIn_2S_4$ showed 70% FDC selectivity[47] and the $MAPbBr_3$ photocatalyst showed 90% FDC selectivity.[76] This might be due to the efficient performance of their dominant reaction species and depends on the reaction conditions such as time of irradiation, mass of the catalyst, and the concentration of HMF. Besides that, titania-based photocatalysts and heterostructures were also reported recently. The enhanced selectivity of FDC was successfully shown with the construction of heterostructure such as SGH-TiO_2,[77] CoOx-Au/TiO_2 (Au 8.0 wt %),[78] and $V_2O_5{\cdot}nH_2O$/g-C_3N_4.[68] SGH-TiO_2 is titania synthesized using sol−gel and hydrothermal-assisted methods. It exhibited an 87% selectivity for FDC at a concentration of 1 mM HMF, while the CoOx-Au/TiO_2 and $V_2O_5{\cdot}nH_2O$/g-C_3N_4 displayed 95% and 87% FDC selectivity using a 0.1 mM HMF concentration. Despite the effect of irradiation time, concentration of HMF and type of light irradiation, the construction of the heterostructure majorly affected the FDC selectivity in a similar manner as presented in this study. The enhanced selectivity of FDC was due to the widened range of the visible-light response, improved charge carrier migration, and the presence of oxygen in photocatalytic oxidation. It can be concluded that the HMF oxidation performance of our CBB/HTiO-NT-30 heterostructures in this work is comparable with other recent photocatalysts in Table S2, without the need to use very expensive (e.g., Au) or highly toxic (e.g., Pb) metals. In BnOH oxidation, the CBB/HTiO-NT-30 in this work converted 97% of BnOH selectively toward BzA (81% selectivity) at 2 h reaction time. In contrast, our recent work reported that the CBHTNS-30 (30 wt % $Cs_3Bi_2Br_9$/HTiO-NS) showed optimal BnOH oxidation performance with 21% BzH and 75% BzA selectivities at 2 h reaction time.[40] The enhancement performance of CBB/HTiO-NT-30 might be due to the geometry and tubular framework of HTiO-NT, which increased the oxidative properties and charge carrier migration in the CBB/HTiO-NT heterostructure. It was reported that the nanotube structure of hydrogen titanate has a channel which provides a geometric confinement for the target molecule and adsorbs it efficiently.[53] The tubular framework of HTiO-NT has quantum confinement effects and large surface area, which restrict the electron and proton migration and enhance its photocatalytic system.[29−31] Huang et al. reported that the 15% $FAPbBr_3/TiO_2$ showed 65% selectivity of BzA for the BnOH photooxidation under 8 h of simulated solar illumination.[79] This work reported that the increased photocatalytic activity of the composite at 15% $FAPbBr_3$ could be attributed to the inherent synergy resulting from the interaction between the composite and the interface. The 15% concentration of $FAPbBr_3$ provided the ideal distance for the migration of the generated charge carriers and avoided excessive exposure of the TiO_2 surface to the reagent solution. Efficient charge separation and reduction of O_2 to generate the superoxide radical depended extensively on the TiO_2 surface. The same pattern can be shown from this work; the CBB/HTiO-NT-30 shows an optimal performance compared to the CBB/HTiO-NT-50, which might be due to the optimal wt % of CBB, which does not overly expose the surface of HTiO-NT to perform the reaction. The conversion to BzA oxidation products was also reported by Du et al., with 91% BnOH conversion, 72.6% BzH and 18.5% BzA selectivity using Au−Pd/$H_2Ti_3O_7$ nanowires photocatalyst.[80] An advantage of our system is that it does not require noble metals. Other studies have also reported similar trends in the BnOH photocatalytic oxidation performance, as shown in Table S2.

Photocatalytic Mechanism. The photocatalytic activity of heterojunction materials is influenced by their optoelectronic properties. As shown in Figure S3, the UV−vis absorption and EIS Nyquist plots were measured to analyze the intrinsic light absorption of the photocatalysts and to explore the photocatalytic mechanism in this system. According to Figure S3a, the absorption edges of HTiO-NT and CBB are located at wavelengths of 368 and 490 nm, respectively. The absorption edge of CBB/HTiO-NT-10 is at 468 nm, while it is 480 nm for both CBB/HTiO-NT-30 and CBB/HTiO-NT-50, indicating that the presence of CBB led to a widened range of the visible-light response.[40] In order to compare the band gap energies of HTiO-NT, CBB, and CBB/HTiO-NT heterostructures with previous studies, the Kubelka−Munk function (eq S5) was employed to generate a Tauc plot and estimate the band gap values. It is important to acknowledge that the Tauc plot generally lacks physical value,[81] but it is possible to draw relative conclusions about light absorption if the materials are compared with one another. Figure S3b displays an illustration of the band gap energy in relation to light energy. The band gap energy of HTiO-NT is 3.38 eV, whereas the band gap of CBB is 2.55 eV. The CBB/HTiO-NT band gap energy ranges from 2.59 to 2.65 eV. These results indicate that HTiO-NT and CBB/HTiO-NT heterostructures effectively absorb visible light, which is beneficial for generating excellent heterostructures and improving charge transfer efficiency.[18,37] Or, in other words, light absorption in the composite is dominated by CBB, as evidenced by the rather similar absorption edge of pure CBB and the composite. The magnitude of the semicircular curve in Nyquist plots (Figure S3c) corresponds to the charge transfer resistance of the electrode surface. A bigger arc radius corresponds to a higher resistance.[82−84] Compared to HTiO-NT and CBB, the CBB/HTiO-NT heterostructure had a notably lower arc resistance ($-Z''$), suggesting superior charge transfer efficiency.[85] The decreased resistance observed in the heterostructure suggests that the tubular framework of HTiO-NT indeed enhances the flow of electrons and protons[29−31] to separate the photogenerated electrons and holes effectively.[85,86] The results are consistent with the photocurrent response investigations described in ref 37, which revealed that

https://doi.org/10.1021/acsanm.4c03998
ACS Appl. Nano Mater. 2024, 7, 25345−25359

the $Cs_3Bi_2Br_9/TiO_2$ heterojunction exhibits a stronger response compared to pure $Cs_3Bi_2Br_9$ and TiO_2. This finding indicates that the creation of a heterojunction can effectively enable the separation of holes and charges, increase the density of the electric current, and optimize the effectiveness of catalysis. Prior studies have used time-resolved photoluminescence (TRPL) measurements to examine carrier dynamics and verify the charge migration between heterostructures or composites. The TRPL results of similar photocatalysts in existing literature, such as $Cs_3Bi_2Br_9/TiO_2$ and $Cs_3Bi_2Br_9/C_3N_4$, support the photoelectrochemical findings presented in this work. The exciton recombination was effectively reduced by the formation of a $Cs_3Bi_2Br_9/TiO_2$ heterojunction, as reported in ref 37. Furthermore, the average lifetime was enhanced from 2.63 to 4.67 ns, demonstrating that the $Cs_3Bi_2Br_9/TiO_2$ heterojunction can facilitate the separation of charges and prevent the recombination of carriers. The rapid transfer of excited electrons from C_3N_4 to $Cs_3Bi_2Br_9$ without recombination was shown in ref 39, indicating that $C_3N_4/Cs_3Bi_2Br_9$ heterostructures enhance charge transfer. The EIS Nyquist plot results (Figure S3c) demonstrate a higher charge transfer efficiency of the CBB/HTiO-NT heterostructures, which is consistent with the findings reported in the literature. In this context as well, the existence of CBB facilitates the separation of charges, suppresses the recombination of carriers, and enhances the carrier transfer.

The capacitance−voltage measurement was conducted to draw the Mott−Schottky plots. The positive slope of Mott−Schottky plots (Figures S 3d) indicated the n-type conductive nature of HTiO-NT with a potential of −0.87 V. As stated in our previous work,[40] the potentials of the conduction band (CB) and valence band (VB) edges of CBB are −0.688 V and +1.862 V, respectively. By using eq S6 and the estimated band gap from the Tauc plot, the potentials of the CB and VB of HTiO-NT were calculated as −0.348 and 3.032 V vs NHE at pH 7, respectively. The calculated VB positions of HTiO-NT were slightly different from previously reported titania at around 2.5 eV[87] and 2.6 V.[88] Scheme 3 illustrates the band

Scheme 3. Schematic Depiction of the Band Structures of HTiO-NT and CBB

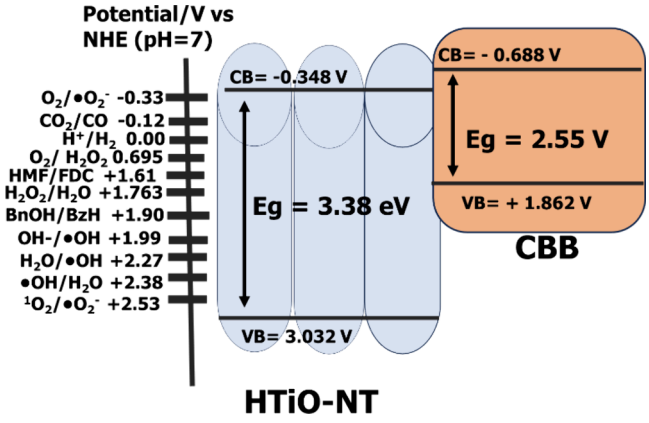

structures of HTiO-NT and CBB. The oxidation of BnOH/BzH and HMF/FDC can be performed at +1.90 V[37,89,90] and +1.61 V,[47,91] respectively. The conduction band (CB) potential of HTiO-NT (−0.348 eV) and of CBB (−0.688 eV) are more negative than that of $O_2/\cdot O_2^-$ (−0.33 V vs NHE at pH 7), so in principle excited electrons in both materials should be able to react with oxygen to generate $\cdot O_2^-$. The CB of CBB is more negative compared to the CB of HTiO-NT, which might be the reason for higher FDC selectivity of CBB compared to HTiO-NT (Figure 5). The VB position of CBB (+1.862 V vs NHE at pH 7) is less positive, while the VB of HTiO-NT (+3.032 V vs NHE at pH 7) is more positive than the standard redox potential of $OH^-/\cdot OH$ (+1.99 V vs NHE at pH 7) and the redox potential of $H_2O/\cdot OH$ (+2.27 V vs NHE at pH 7). Consequently, photoinduced holes of the CBB are thermodynamically unable to generate ·OH radicals, while it is possible for the holes of HTiO-NT to generate the ·OH radicals to contribute to a minor extent to the HMF and BnOH photocatalytic reactions. It is noteworthy that the valence band (VB) maximum of CBB (+1.862 eV) is also appropriate for conducting the oxidation of hydrogen peroxide (H_2O_2) to water (H_2O) at +1.763 eV. This condition could perhaps explain the decomposition of CBB.[40] In conclusion, the tubular framework of HTiO-NT, excellent optical properties of CBB, and the band matching and synergistic interaction between CBB and HTiO-NT led to enhancing the charge density and facilitate the charge carrier migration. The CBB and HTiO-NT may effectively separate photogenerated electrons and holes and actively form $\cdot O_2^-$ at the CB of CBB and slightly ·OH reactive species at the VB of HTiO-NT to enhance the photocatalytic HMF and BnOH oxidation process.

To explore the potential role of reactive species in CBB/HTiO-NT, the results of the scavenger tests were assessed, as shown in Figure 6a. In general, the decrease in photocatalytic efficiency when scavengers were present highlights the significance of reactive species involving photogenerated holes (h^+), photogenerated electrons (e^-), superoxide radicals ($\cdot O_2^-$), and hydroxyl radicals (·OH). Potassium iodide (KI) and silver nitrate ($AgNO_3$), which absorbed the holes (h^+) and electrons (e^-), respectively, had notable impacts with much decreased conversion to 22% and 18%, respectively. The obtained results strongly illustrate the crucial significance of the photoinduced h^+ and photoexcited e^- in this particular process. The e^- has the potential to have a significant impact on initiating the transformation of molecular oxygen into the reactive oxidant species $\cdot O_2^-$ in the catalytic process. Addition of *p*-BQ to the reaction system resulted in a small decrease in HMF conversion to 78%. The selectivity of FDC fell to 55%, suggesting that $\cdot O_2^-$ was not implicated in the initial HMF conversion processes but was contributing to FDC formation, as reported in a prior work.[47] Adding TBA into the reaction system resulted in a modest decrease in HMF conversion (89%), suggesting that ·OH was not the main species involved in the conversion of HMF to FDC. The construction of CBB/HTiO-NT heterostructures revealed advantages in the generation of reactive species, potentially through enhanced charge carrier migration efficiencies, which significantly impact the photocatalytic efficiency. This finding enabled us to deduce that h^+, e^-, and $\cdot O_2^-$, as reactive species, are crucial in the photooxidation of HMF, in line with prior studies.[47,76] Furthermore, it should be emphasized that certain charge carriers (h^+ and ·OH) with adequate oxidation potential to oxidize HMF and BnOH can only be generated on HTiO-NT, not CBB. Identification of reactive oxygen species (such as $^1O_2$ and $\cdot O_2^-$) can be achieved by electron paramagnetic resonance (EPR) spectroscopy. The EPR analysis of similar photocatalysts in the existing literature, such as $Cs_3Bi_2Br_9/TiO_2$, $CsPbBr_3//TiO_2$, and $MAPbBr_3$ perovskite, confirmed the

https://doi.org/10.1021/acsanm.4c03998
ACS Appl. Nano Mater. 2024, 7, 25345−25359

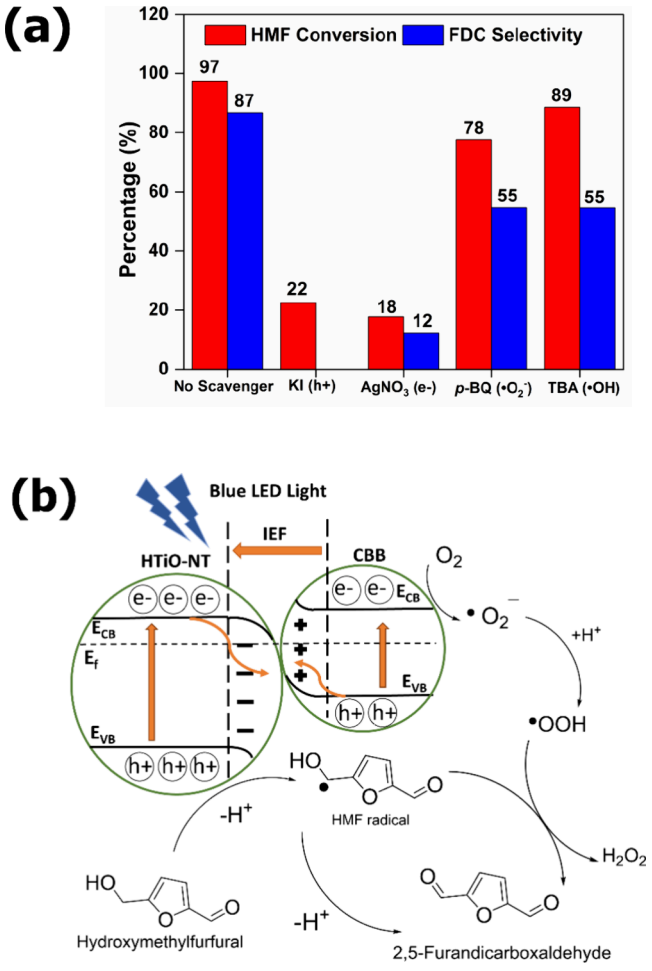

Figure 6. (a) Efficiency of HMF oxidation for CBB/HTiO-NT-30, both with and without scavengers. (b) Schematic representation of the photooxidation of HMF for the CBB/HTiO-NT heterostructure.

findings of our work regarding the scavenger effect. Reference 37 reported the visual observation of the EPR signals of $\cdot O_2^-$ in the presence of light. In contrast, no signals were observed in the absence of light, providing evidence of the photoinduced generation of $\cdot O_2^-$ in the $Cs_3Bi_2Br_9/TiO_2$ composite. Moreover, ref 38 reported that the $CsPbBr_3/TiO_2$ composite exhibited a strong EPR signal when exposed to visible light, in contrast with plain P25. This observation provided confirmation of the generation of $\cdot O_2^-$ radicals. Reference 76 reported that the $MAPbBr_3$ perovskite exhibited EPR signals of TMP−$^1O_2$ and DMPO−$\cdot O_2^-$ when exposed to light. However, no distinct EPR signal was observed in either scenario when the material was in the dark. In conclusion, the presented findings demonstrated the capacity of the perovskite-based photocatalyst to generate reactive oxygen species. These results are consistent with our scavenger findings, which indicated that the $\cdot O_2^-$ has a substantial impact on our HMF photooxidation process. The absorption of light and the activation of charge carriers in photocatalytic redox reactions are constrained by the need that the energy of the light be either equal to or higher than the band gap energy of the photocatalyst. Conduction band (CB) photoexcited electrons demonstrate reductive activity, while valence band (VB) holes display oxidizing capacity. Furthermore, the redox potentials of the processes must match to the positions of the conduction band (CB) and the valence band (VB), which, respectively, indicate the redox potentials of charge carriers activated by light. Thus, based on the present investigation, it is evident that the photooxidation of HMF to FDC in the CBB/HTiO-NT heterostructure can occur through two distinct reaction routes, as illustrated in Figure 6b. Based on the Mott−Schottky curve (Figure S3d), the CB potential of CBB was calculated to be −0.688 V (vs NHE). This indicates that O_2 can be reduced to $\cdot O_2^-$ ($E(O_2/\cdot O_2^-)$ = −0.33 V). A VB potential of +3.032 V (vs NHE) was identified for HTiO-NT, indicating the redox potentials of HMF/FDC (1.61 V) and FDC/oxidized FDC (2.03 V). Blue LED light irradiation at a wavelength of 467 nm enabled the CBB/HTiO-NT heterostructure to absorb light, resulting in the photoexcitation of charge carriers (electron−hole). As previously stated, the photoexcited electrons on the CB of HTiO-NT may also be generated by absorption due to defect sites on HTiO-NT.[92] The rapidly carried photoexcited electrons from the CB of HTiO-NT to the VB of the CBB lead to an accumulation of holes in the VB of HTiO-NT. Photoexcited electrons and holes are spatially separated in the CB of CBB and the VB of HTiO-NT, respectively. A possible route is as follows: The reactant HMF molecule undergoes deprotonation by holes, which rapidly react with adsorbed HMF molecules to generate an intermediate HMF radical and release a single H^+ ion.[47] Afterward, the HMF radicals performed deprotonation to form FDC, therefore releasing the H^+ ion.[93] Another possible route is as follows: Photoexcitation of e^- allows for the activation of molecular O_2 into its reactive superoxide form ($\cdot O_2^-$), which in turn enhances the formation of the hydroperoxyl radical (·OOH) species.[47,76] The ·OOH species may eliminate a proton from the HMF radicals to produce FDC and release H_2O_2.[47,76] The postreaction solution was analyzed using UV−vis DRS to validate our hypothesis. Figure S7 depicts the UV−vis DRS of the postreaction solution without and with the addition of sodium iodide (NaI). The postreaction solution, when including 0.15 g/L of saturated NaI, exhibited an intense yellow coloration (refer to the inset image in Figure S7). Both solutions have a UV−vis absorption peak at wavelengths ranging from 285 to 287 nm, which suggests the existence of HMF molecules.[94] Notably, the solution containing NaI exhibited two absorption peaks at 223 and 350 nm, which correspond to the presence of H_2O_2 and triiodide (I_3^-) species, respectively.[76,95] I_3^- is produced by the electrochemical reaction between H_2O_2 and I^-.[76] In summary, we have demonstrated a practical and environmentally sustainable approach to convert a significant chemical derived from biomass (HMF) into a valuable product of FDC. This is achieved by using CBB/HTiO-NT as a photocatalyst and ambient oxygen as an oxidant while being exposed to blue LED light. Under conditions that are slightly adjusted, the photocatalytic conversion of HMF in an organic solvent reached a selectivity of 97% for HMF and 87% for FDC. Elaborate mechanistic investigations demonstrated that the photogenerated e^-, h^+, and $\cdot O_2^-$ species collectively significantly contribute to the effective and specific oxidation of HMF to FDC. Moreover, the CBB/HTiO-NT photocatalyst was suitable for the photo-oxidation of BnOH, achieving a conversion rate of around 97% and a selectivity of 81% for BzA. The present work introduced a novel method for utilizing a perovskite-based photocatalyst to accomplish the oxidation of HMF and BnOH. Moreover, it may offer useful recommendations on the photocatalytic synthesis of valuable chemicals from biomass waste under mild conditions.

https://doi.org/10.1021/acsanm.4c03998
ACS Appl. Nano Mater. 2024, 7, 25345−25359

CONCLUSION

We successfully enhanced the inadequate reduction capacity of HTiO-NS in our previous study and the mobility of charge carriers in the CBB by the synthesis of a CBB/HTiO-NT heterostructure using a simple method. By employing a modified antisolvent reprecipitation approach, we succeeded in synthesizing CBB/HTiO-NT heterostructures by adding an appropriate proportion of CBB nanoparticles. The aims to widen the range of visible-light response (as compared to the pure HTiO-NT), improve the charge carrier migration, and enhance the oxidative properties of the heterostructure have been achieved, thus enhancing the photocatalytic performance of CBB/HTiO-NT heterostructure. The CBB/HTiO-NT-30 showed the highest HMF and BnOH photooxidation performance with 87% FDC selectivity and 81% BzA selectivity, respectively, in an organic solution reaction under blue light irradiation. Thus, by the effective synthesis and thorough characterization, we revealed the significance of the HTiO-NT and CBB/HTiO-NT heterostructure. In general, the improved photocatalytic performance in this study was due to the (1) tubular framework of HTiO-NT, (2) excellent optical properties of CBB nanoparticles, and (3) the band matching and synergistic interaction between CBB and HTiO-NT, which led to enhancing the charge density to facilitate rapid charge carrier migration. This work proposes an approach for utilizing HTNM-based photocatalysts to improve the charge carrier migration and photocatalytic efficiency of CBB. Moreover, scavenger investigations have shown that the photogenerated h^+ ions, e^-, and $\cdot O_2^-$ species are crucial in the process of HMF photooxidation. This paper provides new ideas for hydrogen titanate-based heterostructures and photocatalytic conversion of biomass to value-added chemicals.

ASSOCIATED CONTENT

Supporting Information

The Supporting Information is available free of charge at https://pubs.acs.org/doi/10.1021/acsanm.4c03998.

Elemental analyses; SEM images of CBB; EDX spectra of CBB; SEM images and elemental mapping of CBB/HTiO-NT-30; N_2 adsorption−desorption isotherms of HTiO-NT and CBB/HTiO-NT heterostructures; photocatalytic performance of BzH and HMF oxidation with different photocatalysts; UV−vis DRS; band gap profile of HTiO-NT, CBB, and CBB/HTiO-NT heterostructures; EIS Nyquist plots of HTiO-NT and CBB; Mott−Schottky plot of HTiO-NT films on FTO; photocatalytic performance of HMF photooxidation toward FDC for all samples at 1.5 h, 10 mg catalyst, and 5 mM concentration of HMF; UV−vis DRS for CBB/HTiO-NT-30 before and after HMF reaction; pXRD for CBB/HTiO-NT-30 before and after HMF reaction; SEM for CBB/HTiO-NT after HMF reaction; UV−vis DRS for postphotocatalytic reaction solution with and without sodium iodide (PDF)

AUTHOR INFORMATION

Corresponding Authors

Tim Peppel − *Leibniz Institute for Catalysis, 18059 Rostock, Germany;* orcid.org/0000-0002-7814-7235; Email: tim.peppel@catalysis.de

Jennifer Strunk − *Leibniz Institute for Catalysis, 18059 Rostock, Germany; School of Natural Sciences, Technical University of Munich (TUM), 85748 Garching, Germany;* orcid.org/0000-0002-6018-3633; Email: jennifer.strunk@tum.de

Authors

Huzaikha Awang − *Leibniz Institute for Catalysis, 18059 Rostock, Germany; Preparatory Centre for Science and Technology, Universiti Malaysia Sabah, 88400 Kota Kinabalu, Sabah, Malaysia;* orcid.org/0000-0001-7824-2825

Abdo Hezam − *School of Natural Sciences, Technical University of Munich (TUM), 85748 Garching, Germany*

Shuoping Ding − *Leibniz Institute for Catalysis, 18059 Rostock, Germany*

Complete contact information is available at: https://pubs.acs.org/10.1021/acsanm.4c03998

Author Contributions

H.A.: Conceptualization, methodology, formal analysis, investigation, writing—original draft preparation, writing—review and editing; S.D.: Methodology; A.H.: Conceptualization, methodology, writing—review and editing, supervision; T.P.: Conceptualization, writing—review and editing, supervision; J.S.: Conceptualization, writing—review and editing, supervision

Notes

The authors declare no competing financial interest.

ACKNOWLEDGMENTS

Huzaikha Awang gratefully acknowledges the scholarship Graduate Excellence Programme (GrEP) provided by Majlis Amanah Rakyat, MARA Malaysia. Shuoping Ding thanks the financial support from the China Scholarship Council (grant no. 201808420272). The Analytical Department of LIKAT is gratefully acknowledged. In addition, the authors thank Hanan Atia (LIKAT), Adwaa Abduh Ali Ahmed (LIKAT), Reinhard Eckelt (LIKAT), Norbert Steinfeldt (LIKAT), Felix Lorenz (LIKAT), and Thi Thanh Hoa Duong (LIKAT) for investigations and discussions. Armin Springer (EMZ Rostock) is gratefully acknowledged for SEM and TEM investigations.

ABBREVIATIONS

SEM, scanning electron microscope; EDX, electron dispersive X-ray spectroscopy; TEM, transmission electron microscopy; HRTEM, high-resolution transmission electron microscopy; pXRD, powder X-ray diffraction; XPS, X-ray photoelectron spectroscopy; BET, Brunauer−Emmett−Teller; HMF, hydroxymethylfurfural; FDC, 2,5-furandicarboxaldehyde; BnOH, benzyl alcohol; BzH, benzaldehyde; BzA, benzoic acid; UV−vis DRS, UV−vis spectroscopy in diffuse reflectance; EIS, electrochemical impedance spectroscopy; CB, conduction band; VB, valence band.

REFERENCES

(1) Yusslee, E.; Beskhyroun, S. The effect of water-to-binder ratio (W/B) on pore structure of one-part alkali activated mortar. *Heliyon* **2023**, *9* (1), No. e12983.

(2) Yusslee, E.; Beskhyroun, S. Performance Evaluation of Hybrid One-Part Alkali Activated Materials (AAMs) for Concrete Structural Repair. *Buildings* **2022**, *12* (11), 2025.

(3) Behnajady, M. A.; Alizade, B. Enhancement of TiO_2-UV100 nanoparticles photocatalytic activity by Mg impregnation in the

removal of a model organic pollutant. *Desalination and Water Treatment* **2015**, *53* (3), 689−696.
(4) Sheng, J.; He, Y.; Li, J.; Yuan, C.; Huang, H.; Wang, S.; Sun, Y.; Wang, Z.; Dong, F. Identification of Halogen-Associated Active Sites on Bismuth-Based Perovskite Quantum Dots for Efficient and Selective CO_2-to-CO Photoreduction. *ACS Nano* **2020**, *14* (10), 13103−13114.
(5) Ali, S. A.; Ahmad, T. Treasure trove for efficient hydrogen evolution through water splitting using diverse perovskite photocatalysts. *Materials Today Chemistry* **2023**, *29*, No. 101387.
(6) Cao, X.; Chen, Z.; Lin, R.; Cheong, W.-C. M.; Liu, S.; Zhang, J.; Peng, Q.; Chen, C.; Han, T.; Tong, X. A photochromic composite with enhanced carrier separation for the photocatalytic activation of benzylic C−H bonds in toluene. *Nature Catalysis* **2018**, *1*, 704.
(7) Yuan, R.; Fan, S.; Zhou, H.; Ding, Z.; Lin, S.; Li, Z.; Zhang, Z.; Xu, C.; Wu, L.; Wang, X.; et al. Chlorine-Radical-Mediated Photocatalytic Activation of C-H Bonds with Visible Light. *Angew. Chem., Int. Ed.* **2013**, *52* (3), 1035−1039.
(8) Somekh, M.; Khenkin, A. M.; Herman, A.; Neumann, R. Selective Visible Light Aerobic Photocatalytic Oxygenation of Alkanes to the Corresponding Carbonyl Compounds. *ACS Catal.* **2019**, *9* (9), 8819−8824.
(9) Song, L.-N.; Ding, F.; Yang, Y.-K.; Ding, D.; Chen, L.; Au, C.-T.; Yin, S.-F. Synthesis of TiO_2/Bi_2MoO_6 Composite for Partial Oxidation of Aromatic Alkanes under Visible-Light Illumination. *ACS Sustainable Chem. Eng.* **2018**, *6* (12), 17044−17050.
(10) Xu, C.; Pan, Y.; Wan, G.; Liu, H.; Wang, L.; Zhou, H.; Yu, S.-H.; Jiang, H.-L. Turning on Visible-Light Photocatalytic C−H Oxidation over Metal−Organic Frameworks by Introducing Metal-to-Cluster Charge Transfer. *J. Am. Chem. Soc.* **2019**, *141* (48), 19110−19117.
(11) Cui, Z.; Wu, Y.; Zhang, S.; Fu, H.; Chen, G.; Lou, Z.; Liu, X.; Zhang, Q.; Wang, Z.; Zheng, Z.; et al. Insight into a strategy to improve charge carrier migration in lead-free bismuth-based halide perovskite for efficient selective oxidation of thioanisole under visible light. *Chemical Engineering Journal* **2023**, *451*, No. 138927.
(12) Cui, Z.; Wang, P.; Wu, Y.; Liu, X.; Chen, G.; Gao, P.; Zhang, Q.; Wang, Z.; Zheng, Z.; Cheng, H.; et al. Space-confined growth of lead-free halide perovskite $Cs_3Bi_2Br_9$ in MCM-41 molecular sieve as an efficient photocatalyst for CO_2 reduction at the gas−solid condition under visible light. *Applied Catalysis B: Environmental* **2022**, *310*, No. 121375.
(13) Yang, B.; Chen, J.; Hong, F.; Mao, X.; Zheng, K.; Yang, S.; Li, Y.; Pullerits, T.; Deng, W.; Han, K. Lead-Free, Air-Stable All-Inorganic Cesium Bismuth Halide Perovskite Nanocrystals. *Angew. Chem., Int. Ed. Engl.* **2017**, *56* (41), 12471−12475.
(14) Wang, Q.; Ma, M.; Cui, K.; Li, X.; Zhou, Y.; Li, Y.; Wu, X. Mechanochemical synthesis of $MAPbBr_3$/carbon sphere composites for boosting carrier-involved superoxide species. *J. Environ. Sci. (China)* **2021**, *104*, 399−414.
(15) Huang, H.; Pradhan, B.; Hofkens, J.; Roeffaers, M. B. J.; Steele, J. A. Solar-Driven Metal Halide Perovskite Photocatalysis: Design, Stability, and Performance. *ACS Energy Letters* **2020**, *5* (4), 1107−1123.
(16) Bai, S.; Jiang, J.; Zhang, Q.; Xiong, Y. Steering charge kinetics in photocatalysis: intersection of materials syntheses, characterization techniques and theoretical simulations. *Chem. Soc. Rev.* **2015**, *44* (10), 2893−2939.
(17) Liu, Z.-L.; Liu, R.-R.; Mu, Y.-F.; Feng, Y.-X.; Dong, G.-X.; Zhang, M.; Lu, T.-B. Lu, T.-B. In Situ Construction of Lead-Free Perovskite Direct Z-Scheme Heterojunction Cs3Bi2I9/Bi2WO6 for Efficient Photocatalysis of CO2 Reduction. *Solar RRL* **2021**, *5* (3), 2000691.
(18) Huang, H.; Yuan, H.; Zhao, J.; Solís-Fernández, G.; Zhou, C.; Seo, J. W.; Hendrix, J.; Debroye, E.; Steele, J. A.; Hofkens, J.; et al. C(sp^3)−H Bond Activation by Perovskite Solar Photocatalyst Cell. *ACS Energy Letters* **2019**, *4* (1), 203−208.
(19) Hezam, A.; Peppel, T.; Strunk, J. Pathways towards a systematic development of Z scheme photocatalysts for CO_2 reduction. *Current Opinion in Green and Sustainable Chemistry* **2023**, *41*, No. 100789.
(20) Soontornchaiyakul, W.; Fujimura, T.; Yano, N.; Kataoka, Y.; Sasai, R. Photocatalytic Hydrogen Evolution over Exfoliated Rh-Doped Titanate Nanosheets. *ACS Omega* **2020**, *5* (17), 9929−9936.
(21) Hareesh, P.; Babitha, K. B.; Shukla, S. Processing fly ash stabilized hydrogen titanate nano-sheets for industrial dye-removal application. *J. Hazard Mater.* **2012**, *229*−*230*, 177−182.
(22) Huang, J.; Cao, Y.; Huang, Q.; He, H.; Liu, Y.; Guo, W.; Hong, M. High-Temperature Formation of Titanate Nanotubes and the Transformation Mechanism of Nanotubes into Nanowires. *Crystal Growth & Design* **2009**, *9*, 3632.
(23) Liu, N.; Chen, X.; Zhang, J.; Schwank, J. W. A review on TiO_2-based nanotubes synthesized via hydrothermal method: Formation mechanism, structure modification, and photocatalytic applications. *Catal. Today* **2014**, *225*, 34−51.
(24) Bokov, D.; Turki Jalil, A.; Chupradit, S.; Suksatan, W.; Javed Ansari, M.; Shewael, I. H.; Valiev, G. H.; Kianfar, E. Nanomaterial by Sol-Gel Method: Synthesis and Application. *Advances in Materials Science and Engineering* **2021**, *2021*, No. 5102014.
(25) Akkerman, Q. A.; Rainò, G.; Kovalenko, M. V.; Manna, L. Genesis, challenges and opportunities for colloidal lead halide perovskite nanocrystals. *Nat. Mater.* **2018**, *17* (5), 394−405.
(26) Mekuye, B.; Abera, B. Nanomaterials: An overview of synthesis, classification, characterization, and applications. *Nano Select* **2023**, *4* (8), 486−501.
(27) Afolalu, S. A.; Soetan, S. B.; Ongbali, S. O.; Abioye, A. A.; Oni, A. S. Morphological characterization and physio-chemical properties of nanoparticle - review. *IOP Conference Series: Materials Science and Engineering* **2019**, *640* (1), No. 012065.
(28) De, M.; Ghosh, P. S.; Rotello, V. M. Applications of Nanoparticles in Biology. *Adv. Mater.* **2008**, *20* (22), 4225−4241.
(29) Pauzauskie, P. J.; Yang, P. Nanowire photonics. *Mater. Today* **2006**, *9* (10), 36−45.
(30) Yan, R.; Gargas, D.; Yang, P. Nanowire photonics. *Nat. Photonics* **2009**, *3* (10), 569−576.
(31) Lei, E.; Hu, C.; Hu, K.; Zhao, W.; Cui, J.; Xiong, Q.; Guo, Z.; Liu, Z. Composition, morphology, structure and photocatalytic performances of photocatalysts prepared from titanium potassium oxalate. *Solid State Sci.* **2019**, *88*, 36−40.
(32) Gao, T.; Fjellvag, H.; Norby, P. Crystal Structures of Titanate Nanotubes: A Raman Scattering Study. *Inorg. Chem.* **2009**, *48*, 1423−1432.
(33) Chen, X.; Cao, S.; Weng, X.; Wang, H.; Wu, Z. Effects of morphology and structure of titanate supports on the performance of ceria in selective catalytic reduction of NO. *Catal. Commun.* **2012**, *26*, 178−182.
(34) Chen, X.; Mao, S. S. Titanium Dioxide Nanomaterials: Synthesis, Properties, Modifications, and Applications. *Chem. Rev.* **2007**, *107* (7), 2891−2959.
(35) Padmanabhan, N. T.; John, H. Titanium dioxide based self-cleaning smart surfaces: A short review. *Journal of Environmental Chemical Engineering* **2020**, *8* (5), No. 104211.
(36) Schünemann, S.; van Gastel, M.; Tüysüz, H. A $CsPbBr_3/TiO_2$ Composite for Visible-Light-Driven Photocatalytic Benzyl Alcohol Oxidation. *ChemSusChem* **2018**, *11* (13), 2057−2061.
(37) Sun, Q.; Ye, W.; Wei, J.; Li, L.; Wang, J.; He, J.-H.; Lu, J.-M. Lead-free perovskite $Cs_3Bi_2Br_9$ heterojunctions for highly efficient and selective photocatalysis under mild conditions. *J. Alloys Compd.* **2022**, *893*, No. 162326.
(38) Schünemann, S.; van Gastel, M.; Tüysüz, H. A $CsPbBr_3$ /TiO_2 Composite for Visible-Light-Driven Photocatalytic Benzyl Alcohol Oxidation. *ChemSusChem* **2018**, *11* (13), 2057−2061.
(39) Xu, W.-L.; Hu, J.; Yang, Q.; Lian, Y.; Zheng, M.; Du, E. Charge transfer dynamics in C3N4 encapsulated Cs3Bi2Br9 nanocrystals heterojunction for photocatalytic application. *J. Alloys Compd.* **2024**, *988*, 174275.

https://doi.org/10.1021/acsanm.4c03998
ACS Appl. Nano Mater. 2024, 7, 25345−25359

(40) Awang, H.; Hezam, A.; Peppel, T.; Strunk, J. Enhancing the Photocatalytic Activity of Halide Perovskite Cesium Bismuth Bromide/Hydrogen Titanate Heterostructures for Benzyl Alcohol Oxidation. *Nanomaterials* **2024**, *14*, 752.
(41) Ding, D.; Wang, J.; Xi, J.; Liu, X.; Lu, G.; Wang, Y. High-yield production of levulinic acid from cellulose and its upgrading to γ-valerolactone. *Green Chem.* **2014**, *16* (8), 3846−3853.
(42) Xie, T.; Yue, S.; Su, T.; Song, M.; Xu, W.; Xiao, Y.; Yang, Z.; Len, C.; Zhao, D. High selective oxidation of 5-hydroxymethyl furfural to 5-hydroxymethyl-2-furan carboxylic acid using Ag-TiO_2. *Molecular Catalysis* **2022**, *525*, No. 112353.
(43) Zhang, Z.; Deng, K. Recent Advances in the Catalytic Synthesis of 2,5-Furandicarboxylic Acid and Its Derivatives. *ACS Catal.* **2015**, *5*, 6529−6544.
(44) Zhang, Q.; Zhang, H.; Gu, B.; Tang, Q.; Cao, Q.; Fang, W. Sunlight-driven photocatalytic oxidation of 5-hydroxymethylfurfural over a cuprous oxide-anatase heterostructure in aqueous phase. *Applied Catalysis B: Environmental* **2023**, *320*, No. 122006.
(45) Ilkaeva, M.; Krivtsov, I.; García, J. R.; Díaz, E.; Ordóñez, S.; García-López, E. I.; Marcì, G.; Palmisano, L.; Maldonado, M. I.; Malato, S. Selective photocatalytic oxidation of 5-hydroxymethyl-2-furfural in aqueous suspension of polymeric carbon nitride and its adduct with H_2O_2 in a solar pilot plant. *Catal. Today* **2018**, *315*, 138−148.
(46) Lima, M. J.; Tavares, P. B.; Silva, A. M. T.; Silva, C. G.; Faria, J. L. Selective photocatalytic oxidation of benzyl alcohol to benzaldehyde by using metal-loaded g-C_3N_4 photocatalysts. *Catal. Today* **2017**, *287*, 70−77.
(47) Ding, S.; Gabriel Filho, J. B.; Peppel, T.; Haida, S.; Rabeah, J.; Steinfeldt, N.; Strunk, J. Selective oxidation of 5-hydroxymethylfurfural to 2,5-diformylfuran with $ZnIn_2S_4$ 2D nanosheets and atmospheric O_2 under visible light. *Sustainable Energy & Fuels* **2023**, *7* (18), 4396−4400.
(48) Chen, Y.; Yang, S.; Wang, K.; Lou, L. Role of primary active species and TiO_2 surface characteristic in UV-illuminated photodegradation of Acid Orange 7. *J. Photochem. Photobiol., A* **2005**, *172* (1), 47−54.
(49) Higashimoto, S.; Suetsugu, N.; Azuma, M.; Ohue, H.; Sakata, Y. Efficient and selective oxidation of benzylic alcohol by O_2 into corresponding aldehydes on a TiO_2 photocatalyst under visible light irradiation: Effect of phenyl-ring substitution on the photocatalytic activity. *J. Catal.* **2010**, *274* (1), 76−83.
(50) Zhao, L.; Zhang, B.; Xiao, X.; Gu, F. L.; Zhang, R.-Q. Roles of the active species involved in the photocatalytic oxidation of benzyl alcohol into benzaldehyde on TiO_2 under UV light: Experimental and DFT studies. *J. Mol. Catal. A: Chem.* **2016**, *420*, 82−87.
(51) Kasuga, T.; Hiramatsu, M.; Hoson, A.; Sekino, T.; Niihara, K. Formation of titanium oxide nanotube. *Langmuir* **1998**, *14*, 3160−3163.
(52) Alkanad, K.; Hezam, A.; Al-Zaqri, N.; Bajiri, M. A.; Alnaggar, G.; Drmosh, Q. A.; Almukhlifi, H. A.; Neratur Krishnappagowda, L. One-Step Hydrothermal Synthesis of Anatase TiO_2 Nanotubes for Efficient Photocatalytic CO_2 Reduction. *ACS Omega* **2022**, *7* (43), 38686−38699.
(53) Deng, Q.; Huang, C.; Xie, W.; Zhang, J.; Zhao, Y.; Hong, Z.; Pang, A.; Wei, M. Significant reduction of harmful compounds in tobacco smoke by the use of titanate nanosheets and nanotubes. *Chem. Commun.* **2011**, *47* (21), 6153−6155.
(54) Cao, Y.; Zhang, Z.; Li, L.; Zhang, J.-R.; Zhu, J.-J. An Improved Strategy for High-Quality Cesium Bismuth Bromine Perovskite Quantum Dots with Remarkable Electrochemiluminescence Activities. *Anal. Chem.* **2019**, *91* (13), 8607−8614.
(55) Masri, M.; Girisha, K. B.; Hezam, A.; Qahtan, T. F.; Alkanad, K.; Masri, F.; Namratha, K.; Udayabhanu; Byrappa, K. Enhanced photocatalytic activity and stability of 2D $Cs_3Bi_2Br_9$ perovskite nanosheets synthesized via modified antisolvent method. *Colloids and Surfaces C: Environmental Aspects* **2024**, *2*, 100024.
(56) Wu, L.; Yang, X.; Li, J.; Huang, Y.; Li, X. Fabrication of titanium dioxide nanotubes with good morphology at high calcination temperature and their photocatalytic activity. *Mater. Chem. Phys.* **2017**, *202*, 136−142.
(57) Parayil, S. K.; Baltrusaitis, J.; Wu, C.-M.; Koodali, R. T. Synthesis and characterization of ligand stabilized CdS-Trititanate composite materials for visible light-induced photocatalytic water splitting. *Int. J. Hydrogen Energy* **2013**, *38* (6), 2656−2669.
(58) Rutar, M.; Rozman, N.; Pregelj, M.; Bittencourt, C.; Cerc Korošec, R.; Škapin, A.; Mrzel, A.; Skapin, S.; Umek, P. Transformation of hydrogen titanate nanoribbons to TiO_2 nanoribbons and the influence of the transformation strategies on the photocatalytic performance. *Beilstein journal of nanotechnology* **2015**, *6*, 831−844.
(59) Chen, Q.; Zhou, W.; Du, G. H.; Peng, L. M. Trititanate Nanotubes Made via a Single Alkali Treatment. *Adv. Mater.* **2002**, *14* (17), 1208−1211.
(60) Sarma, D.; Malliakas, C. D.; Subrahmanyam, K. S.; Islam, S. M.; Kanatzidis, M. G. $K_{2x}Sn_{4-x}S_{8-x}$ (x = 0.65−1): a new metal sulfide for rapid and selective removal of Cs^+, Sr^{2+} and UO_2^{2+} ions. *Chemical Science* **2016**, *7* (2), 1121−1132.
(61) Yang, F.; Elnabawy, A. O.; Schimmenti, R.; Song, P.; Wang, J.; Peng, Z.; Yao, S.; Deng, R.; Song, S.; Lin, Y.; et al. Bismuthene for highly efficient carbon dioxide electroreduction reaction. *Nat. Commun.* **2020**, *11* (1), 1088.
(62) Rakibuddin, M.; Kim, H. Reduced graphene oxide supported C_3N_4 nanoflakes and quantum dots as metal-free catalysts for visible light assisted CO_2 reduction. *Beilstein J. Nanotechnol* **2019**, *10*, 448−458.
(63) Li, Q.; Song, T.; Zhang, Y.; Wang, Q.; Yang, Y. Boosting Photocatalytic Activity and Stability of Lead-Free $Cs_3Bi_2Br_9$ Perovskite Nanocrystals via In Situ Growth on Monolayer 2D $Ti_3C_2T_x$ MXene for C−H Bond Oxidation. *ACS Appl. Mater. Interfaces* **2021**, *13* (23), 27323−27333.
(64) Liu, E.; Lin, X.; Hong, Y.; Yang, L.; Luo, B.; Shi, W.; Shi, J. Rational copolymerization strategy engineered C self-doped g-C_3N_4 for efficient and robust solar photocatalytic H2 evolution. *Renewable energy* **2021**, *178*, 757.
(65) Wang, C.; Fan, H.; Ren, X.; Fang, J.; Ma, J.; Zhao, N. Porous graphitic carbon nitride nanosheets by pre-polymerization for enhanced photocatalysis. *Mater. Charact.* **2018**, *139*, 89−99.
(66) Hua, S.; Yu, X.; Li, F.; Duan, J.; Ji, H.; Liu, W. Hydrogen titanate nanosheets with both adsorptive and photocatalytic properties used for organic dyes removal. *Colloids Surf., A* **2017**, *516*, 211−218.
(67) Bresolin, B.-M.; Balayeva, N. O.; Granone, L. I.; Dillert, R.; Bahnemann, D. W.; Sillanpää, M. Anchoring lead-free halide $Cs_3Bi_2I_9$ perovskite on UV100−TiO_2 for enhanced photocatalytic performance. *Sol. Energy Mater. Sol. Cells* **2020**, *204*, No. 110214.
(68) Wang, H.; Huang, D.; Zhuge, Q.; Wu, Y. Oxygen vacancies mediated enhanced visible-light-driven photocatalytic oxidation of biomass derived 5-hydroxymethylfurfural over $V_2O_5{\cdot}nH_2O$/g-C_3N_4 composite. *Diamond Relat. Mater.* **2023**, *139*, No. 110413.
(69) Uddin, A.; Upama, M. B.; Yi, H.; Duan, L. Encapsulation of Organic and Perovskite Solar Cells: A Review. *Coatings* **2019**, *9* (2), 65.
(70) Kore, B. P.; Jamshidi, M.; Gardner, J. M. The impact of moisture on the stability and degradation of perovskites in solar cells. *Materials Advances* **2024**, *5* (6), 2200−2217.
(71) Hiragond, C. B.; Powar, N. S.; In, S.-I. Recent Developments in Lead and Lead-Free Halide Perovskite Nanostructures towards Photocatalytic CO_2 Reduction. *Nanomaterials* **2020**, *10* (12), 2569.
(72) Huang, J.; Lei, T.; Siron, M.; Zhang, Y.; Yu, S.; Seeler, F.; Dehestani, A.; Quan, L. N.; Schierle-Arndt, K.; Yang, P. Lead-free Cesium Europium Halide Perovskite Nanocrystals. *Nano Lett.* **2020**, *20* (5), 3734−3739.
(73) Noel, N. K.; Habisreutinger, S. N.; Pellaroque, A.; Pulvirenti, F.; Wenger, B.; Zhang, F.; Lin, Y.-H.; Reid, O. G.; Leisen, J.; Zhang, Y.; et al. Interfacial charge-transfer doping of metal halide perovskites for high performance photovoltaics. *Energy Environ. Sci.* **2019**, *12* (10), 3063−3073.

https://doi.org/10.1021/acsanm.4c03998
ACS Appl. Nano Mater. 2024, 7, 25345−25359

(74) Liu, J.; Wu, Y.; Qin, C.; Yang, X.; Yasuda, T.; Islam, A.; Zhang, K.; Peng, W.; Chen, W.; Han, L. A dopant-free hole-transporting material for efficient and stable perovskite solar cells. *Energy Environ. Sci.* **2014**, *7* (9), 2963−2967.
(75) Docampo, P.; Bein, T. A Long-Term View on Perovskite Optoelectronics. *Acc. Chem. Res.* **2016**, *49* (2), 339−346.
(76) Zhang, M.; Li, Z.; Xin, X.; Zhang, J.; Feng, Y.; Lv, H. Selective Valorization of 5-Hydroxymethylfurfural to 2,5-Diformylfuran Using Atmospheric O_2 and $MAPbBr_3$ Perovskite under Visible Light. *ACS Catal.* **2020**, *10* (24), 14793−14800.
(77) Khan, A.; Goepel, M.; Kubas, A.; Łomot, D.; Lisowski, W.; Lisovytskiy, D.; Nowicka, A.; Colmenares, J. C.; Gläser, R. Selective Oxidation of 5-Hydroxymethylfurfural to 2,5-Diformylfuran by Visible Light-Driven Photocatalysis over In Situ Substrate-Sensitized Titania. *ChemSusChem* **2021**, *14* (5), 1351−1362.
(78) Yang, W.; Fu, M.; Yang, C.; Zhang, Y.; Shen, C. $Au^{\delta-}$−O_v−Ti^{3+}: Active site of MO_x-Au/TiO_2 catalysts for the aerobic oxidation of 5-hydroxymethylfurfural. *Green Energy & Environment* **2023**, *8* (3), 785−797.
(79) Huang, H.; Yuan, H.; Janssen, K. P. F.; Solís-Fernández, G.; Wang, Y.; Tan, C. Y. X.; Jonckheere, D.; Debroye, E.; Long, J.; Hendrix, J.; et al. Efficient and Selective Photocatalytic Oxidation of Benzylic Alcohols with Hybrid Organic−Inorganic Perovskite Materials. *ACS Energy Letters* **2018**, *3* (4), 755−759.
(80) Du, M.; Zeng, G.; Huang, J.; Sun, D.; Li, Q.; Wang, G.; Li, X. Green Photocatalytic Oxidation of Benzyl Alcohol over Noble-Metal-Modified $H_2Ti_3O_7$ Nanowires. *ACS Sustainable Chem. Eng.* **2019**, *7* (10), 9717−9726.
(81) Klein, J.; Kampermann, L.; Mockenhaupt, B.; Behrens, M.; Strunk, J.; Bacher, G. Limitations of the Tauc Plot Method. *Adv. Funct. Mater.* **2023**, *33* (47), 2304523 DOI: 10.1002/adfm.202304523.
(82) You, Q.; Zhang, Q.; Gu, M.; Du, R.; Chen, P.; Huang, J.; Wang, Y.; Deng, S.; Yu, G. Self-assembled graphitic carbon nitride regulated by carbon quantum dots with optimized electronic band structure for enhanced photocatalytic degradation of diclofenac. *Chemical Engineering Journal* **2022**, *431*, No. 133927.
(83) Leelavathi, A.; Madras, G.; Ravishankar, N. New Insights into Electronic and Geometric Effects in the Enhanced Photoelectrooxidation of Ethanol Using ZnO Nanorod/Ultrathin Au Nanowire Hybrids. *J. Am. Chem. Soc.* **2014**, *136* (41), 14445−14455.
(84) Awang, H.; Peppel, T.; Strunk, J. Photocatalytic Degradation of Diclofenac by Nitrogen-Doped Carbon Quantum Dot-Graphitic Carbon Nitride (CNQD). *Catalysts* **2023**, *13*, 735.
(85) Seng, R. X.; Tan, L.-L.; Lee, W. P. C.; Ong, W.-J.; Chai, S.-P. Nitrogen-doped carbon quantum dots-decorated 2D graphitic carbon nitride as a promising photocatalyst for environmental remediation: A study on the importance of hybridization approach. *Journal of Environmental Management* **2020**, *255*, No. 109936.
(86) Shi, L.; Chang, K.; Huabin, Z.; Hai, X.; Yang, L.; Wang, T.; Ye, J. Drastic Enhancement of Photocatalytic Activities over Phosphoric Acid Protonated Porous g-C3N4 Nanosheets under Visible Light. *Small* **2016**, *12*, 4431.
(87) Camposeco, R.; Castillo, S.; Rodriguez-González, V.; Hinojosa-Reyes, M.; Medina-Alvares, M. I.; Mejía-Centeno, I. Promotional effect of Rh nanoparticles on WO_3/TiO_2 titanate nanotube photocatalysts for boosted hydrogen production. *J. Photochem. Photobiol., A* **2018**, *353*, 114−121.
(88) Błędowski, M.; Wang, L.; Ramakrishnan, A.; Khavryuchenko, O.; Khavryuchenko, V.; Ricci, P. C.; Strunk, J.; Cremer, T.; Kolbeck, C.; Beranek, R. Visible-light photocurrent response of TiO_2-polyheptazine hybrids: Evidence for interfacial charge-transfer absorption. *Physical chemistry chemical physics: PCCP* **2011**, *13*, 21511−21519.
(89) Jin, J.; Huang, H.; Chen, C.; Smith, P. W.; Folgueras, M. C.; Yu, S.; Zhang, Y.; Chen, P.-C.; Seeler, F.; Schaefer, B.; et al. Benzyl Alcohol Photo-oxidation Based on Molecular Electronic Transitions in Metal Halide Perovskites. *ACS Photonics* **2023**, *10* (3), 772−779.
(90) Xiong, L.; Tang, J. Strategies and Challenges on Selectivity of Photocatalytic Oxidation of Organic Substances. *Adv. Energy Mater.* **2021**, *11* (8), 2003216.
(91) Wang, X.-X.; Meng, S.; Zhang, S.; Zheng, X.; Chen, S. 2D/2D MXene/g-C3N4 for photocatalytic selective oxidation of 5-hydroxymethylfurfural into 2,5-formylfuran. *Catal. Commun.* **2020**, *147*, 106152.
(92) Banerjee, A. N.; Anitha, V. C.; Joo, S. W. Improved electrochemical properties of morphology-controlled titania/titanate nanostructures prepared by in-situ hydrothermal surface modification of self-source Ti substrate for high-performance supercapacitors. *Sci. Rep.* **2017**, *7* (1), 13227.
(93) Meng, S.; Wu, H.; Cui, Y.; Zheng, X.; Wang, H.; Chen, S.; Wang, Y.; Fu, X. One-step synthesis of 2D/2D-3D NiS/$Zn_3In_2S_6$ hierarchical structure toward solar-to-chemical energy transformation of biomass-relevant alcohols. *Applied Catalysis B: Environmental* **2020**, *266*, No. 118617.
(94) Adu, J. K.; Amengor, C. D. K.; Orman, E.; Ibrahim, N. M.; Ifunanya, M. O.; Arthur, D. F. Development and Validation of UV-Visible Spectrophotometric Method for the Determination of 5-Hydroxymethyl Furfural Content in Canned Malt Drinks and Fruit Juices in Ghana. *Journal of Food Quality* **2019**, *2019*, 1.
(95) Aye, T.; Low, T.; Sze, S. Nanosecond Laser-Induced Photochemical Oxidation Method for Protein Surface Mapping with Mass Spectrometry. *Analytical chemistry* **2005**, *77*, 5814−5822.

https://doi.org/10.1021/acsanm.4c03998
ACS Appl. Nano Mater. 2024, 7, 25345−25359